Subduction of inorganic and organic carbon in the Southern Ocean in an eddying ocean model

Simone Le Chevère

Department of Atmospheric and Oceanic Sciences
McGill University, Montreal

August 15^{th}, 2023

Supervisor : Carolina Dufour

A thesis submitted to McGill University in partial fulfillment of the requirements of the degree of Master of Science in Atmospheric and Oceanic Sciences

Abstract

The Southern Ocean (SO - south of 35°S) represents a small source of natural carbon for the atmosphere but a major sink of anthropogenic carbon (about 40% of the global ocean anthropogenic carbon sink). The strength of the total carbon sink that results from these two components strongly depends on the rate of carbon subduction through the base of the mixed layer. Quantifying carbon subduction rates is therefore essential to estimate how much carbon is stored sustainably in the ocean. Despite the recent increase in measurements of physical and biogeochemical variables in the Southern Ocean provided by the BGC-Argo floats, observations in this remote region are still insufficient to perform reliable estimates of carbon subduction rates. Therefore many questions remain on the drivers of these subduction rates as well as on their spatial and temporal variability. Here, we examine historical and anthropogenic carbon subduction fluxes at the base of the mixed layer using a global ocean model with a nominal resolution of 0.25° (∼5 km in the Southern Ocean) based on the NEMO model platform and coupled to the biogeochemical component PISCES. Two simulations are analyzed, one with pre-industrial atmospheric and oceanic carbon concentrations, and a second that follows historical carbon concentrations. The difference between the two simulations provides the anthropogenic carbon component. Online diagnostics of subduction fluxes of inorganic carbon and organic carbon across the base of the mixed layer are performed and analyzed over five regions of the Southern Ocean to identify the underlying processes of the carbon transfer to and from the ocean interior. For each region, subduction rates and estimates of fluxes across the region boundaries are used to compute a carbon budget. Historical carbon is mostly taken up and then subducted north of the ACC, while obduction occurs south of the Antarctic Circumpolar Current (ACC) through upwelling, for a net obduction of 11.6 PgC/year over the Southern Ocean. Advection dominates the transfer of historical carbon with a contribution of 67% to the total transfer. We find that, while the air-sea fluxes of anthropogenic carbon are important both north and south of the ACC, anthropogenic carbon is mainly subducted in the north, the carbon absorbed in the south being advected northward within the mixed layer. The anthropogenic carbon uptaken at the sea surface of the SO represents 81% of the carbon subducted at depth, the remaining 19% coming from subtropical regions north of 35°S. Subduction occurs mainly through advection and diffusion, each process contributing almost equally to the total subduction. Organic carbon subduction is found to be of the same magnitude as anthropogenic inorganic carbon subduction and is also transported through the mixed layer by advective and diffusive processes. This physical transfer, though half the size of the gravitational pump,

appears significant and should not be neglected. Overall, our results highlight the major role of advective processes in the transfer of inorganic and organic carbon to the ocean interior, with this predominance of advective processes likely arising from the ability of the model to partly resolve the mesocale dynamics.

Résumé

L'océan Austral (au sud de 35°S) représente une petite source de carbone naturel pour l'atmosphère mais un puits majeur de carbone anthropique (environ 40% du puits de carbone anthropique de l'océan mondial). L'importance du puits de carbone total qui résulte de ces deux composantes dépend fortement du taux de subduction du carbone à travers la base de la couche de mélange. La quantification des taux de subduction du carbone est donc essentielle pour estimer la quantité de carbone stockée durablement dans l'océan. Malgré l'augmentation récente des mesures de variables physiques et biogéochimiques dans l'océan Austral fournies par les flotteurs BGC-Argo, les observations dans cette région éloignée sont encore insuffisantes pour effectuer des estimations fiables des taux de subduction du carbone. De nombreuses questions subsistent donc sur les moteurs de ces taux de subduction ainsi que sur leur variabilité spatiale et temporelle. Ici, nous examinons les flux de subduction de carbone historiques et anthropiques à la base de la couche de mélange à l'aide d'un modèle océanique global avec une résolution nominale de 0,25° (∼5 km dans l'océan Austral) basé sur la plate-forme de modélisation de l'océan NEMO, couplé à la composante biogéochimique PISCES. Deux simulations sont analysées, une avec des concentrations de carbone atmosphérique et océanique préindustrielles, et l'autre qui suit les concentrations de carbone historiques. La différence entre les deux simulations fournit la composante de carbone anthropique. Des diagnostics en ligne des flux de subduction de carbone inorganique et de carbone organique à travers la base de la couche de mélange sont effectués et analysés sur cinq régions de l'océan Austral pour identifier les processus sous-jacents du transfert de carbone vers et depuis l'intérieur de l'océan. Pour chaque région, les taux de subduction et les estimations des flux à travers les frontières des régions sont utilisés pour calculer des bilans de carbone. Le carbone historique est principalement absorbé puis subducté au nord du Courant Circumpolaire Antarctique (ACC), tandis que l'obduction se produit au sud de l'ACC par remontée d'eau, pour une obduction nette de 11,6 PgC/an sur l'océan Austral. L'advection domine le transfert de carbone historique avec une contribution de 67% au transfert total. Nous constatons qu'alors que les flux air-mer de carbone anthropique sont importants à la fois au nord et au sud de l'ACC, le carbone anthropique est principalement subducté au nord, le carbone absorbé au sud étant advecté vers le nord dans la couche de mélange. Le carbone anthropique capté à la surface de l'océan Austral représente 81% du carbone subducté en profondeur, les 19% restants provenant des régions subtropicales au nord de 35°S. La subduction se produit principalement par advection et diffusion, chaque

processus contribuant à part presque égale à la subduction totale. La subduction du carbone organique s'avère être de la même ampleur que la subduction du carbone inorganique anthropique et est également effectuée à travers la couche de mélange par des processus d'advection et de diffusion. Ce transfert physique, bien que deux fois plus faible que celui de la pompe gravitationnelle, apparaît important et ne doit pas être négligé. La subduction du carbone organique a le même ordre de grandeur que la subduction du carbone inorganique anthropique. Dans l'ensemble, nos résultats mettent en évidence le rôle majeur des processus d'advection dans le transfert de carbone inorganique et organique vers l'intérieur de l'océan, cette prédominance des processus d'advection résultant probablement de la capacité du modèle à résoudre en partie la dynamique de méso-échelle.

Acknowledgements

First I would like to thank my supervisor Carolina Dufour, who gave me all the guidelines necessary for my work, constant feedback, and all the support needed. She has funded me during my master, through her NSERC grant. I also received financial support from the McGill AOS department, through various scholarships and travel awards. I would also like to acknowledge the co-supervision by Laurent Bopp from the LMD-ISPL and Marina Lévy from the LOCEAN-IPSL, who gave me the simulations and the main idea on which I base this work, and close supervision with frequent online meetings. Thank you very much for your support. I would like to thank again Carolina for allowing and encouraging me to participate in the course and research cruise OTC23, given by the European Spatial Agency and the Nansen Center, and in three conferences, Ocean Sciences 2022, the Réunion Scientifique Annuelle of Québec Océan 2023 and the SOCCOM Annual Meeting 2023. Marina also allowed me to participate virtually in the SOLACE workshop in November 2022.

Many thanks to Eric Galbraith for reviewing my thesis and giving me very useful feedback.

I would like to acknowledge both the AOS Department of McGill and the IPSL for their numerical resources. I used the NEMO-PISCES simulations run by Christian Ethé from the LOCEAN-IPSL. He gave me a lot of information on the simulations I was using. I really thank Olivier Torres from the LMD-IPSL, for transferring all the simulation outputs for me and giving me technical support during my master to be able to use the SPIRIT server of IPSL. On the same note, many thanks to Ambrish Raghoonundun from McGill University, who solved all my technical problems at McGill University.

I am very grateful to our group in AOS, Esteban, Jan, Mathilde, Noemie and Siwen, who were very helpful. I really appreciated having a very nice group cohesion.

Finally, I would like to thank the AOS department: the administration who was very helpful, the professors who gave me guidance and especially all my friends and classmates who were very supportive during these two years.

Contribution of authors

The thesis was conceived by Laurent Bopp, Marina Lévy, and Carolina Dufour. The simulations used in this thesis were run by Christian Ethé, and the outputs were transferred to the server used for data analysis by Olivier Torres. The data analyses and writing of the manuscript were done by Simone Le Chevère, under the supervision of Carolina Dufour. Carolina Dufour, Laurent Bopp and Marina Lévy contributed to interpret the results. Carolina Dufour revised the manuscript. A paper based on this thesis is in preparation for Global Biogeochemical Cycles.

List of figures and tables

List of abbreviations

AABW Antarctic Bottom Waters. 14

AAIW Antarctic Intermediate Water. 14

ACC Antarctic Circumpolar Current. 14

ASZ Antarctic Southern Zone. 23

CDW Circumpolar Deep Waters. 14

DIC Dissolved Inorganic Carbon. 14

DIC_{anth} Anthropogenic Dissolved Inorganic Carbon. 41

DIC_{hist} Historical Dissolved Inorganic Carbon. 36

DOC Dissolved Organic Carbon. 15

EKE Eddy Kinetic Energy. 75

LIM Louvain-la-Neuve sea Ice Model. 20

MLD Mixed Layer Depth. 28

NEMO Nucleus for European Modelling of the Ocean. 20

NPP Net Primary Production. 46

OPA Parallelized Ocean. 20

PF Polar Front. 23

PFZ Polar Frontal Zone. 24

PIC Particulate Inorganic Carbon. 15

PISCES Pelagic Interaction Scheme for Carbon and Ecosystem Studies. 20

POC Particulate Organic Carbon. 15

SAF Subantarctic Front. 24

SAMW Subantarctic Mode Waters. 14

SAZ Subantarctic Zone. 24

SIF Sea Ice Front. 23

SIZ Sea Ice Zone. 23

SO Southern Ocean. 14

SOCAT Surface Ocean CO_2 Atlas. 23

SOCCOM Southern Ocean Carbon and Climate Observations and Modeling. 23

SSH Sea Surface Height. 23

STF Subtropical Front. 24

STW Subtropical Waters. 14

STZ Subtropical Zone. 24

TOC Total Organic Carbon. 15

WOA13 World Ocean Atlas 2013. 23

Contents

Chapter 1

Introduction

The Southern Ocean (SO) plays a dominant role in the global carbon cycle, as it is both a source of natural (preindustrial) carbon to the atmosphere in winter and a major sink of anthropogenic carbon (about 40% of the global ocean anthropogenic carbon sink) (Gruber et al., 2019b; Frölicher et al., 2015; DeVries, 2014; Sabine, 2004). This disproportionately large subduction of anthropogenic carbon in the SO (considering the SO represents only 20% of the ocean's surface south of 35°S Gruber et al. (2019b)) is mainly achieved thanks to the SO unique circulation Marshall and Speer (2012); Lumpkin and Speer (2007) (Fig.1.1). Within and south of the Antarctic Circumpolar Current (ACC), the Circumpolar Deep waters (CDW), which are rich in preindustrial dissolved inorganic carbon (DIC) accumulated through remineralization, upwell, leading to significant outgassing in the winter (Gray et al., 2018; Talley, 2013; Mikaloff Fletcher et al., 2007). In contrast, CDW are poor in anthropogenic carbon due to the lack of exposure to the contemporary atmosphere (Graven et al., 2012; Orr et al., 2001). As a result, CDW absorb large amounts of anthropogenic carbon where they upwell (Toyama et al., 2017; Mikaloff Fletcher et al., 2006; Sarmiento et al., 1992). Part of the upwelled waters heads towards the South, where they contribute to the formation of Dense Shelf Waters and Antarctic Bottom Waters (AABW) in the Antarctic margins; the other part heads towards the North and, as they become lighter, transform into Antarctic Intermediate Water (AAIW) and Subantarctic Mode Waters (SAMW) to eventually subduct below Subtropical Waters (STW), bringing with them the absorbed carbon.

The efficiency of the SO carbon sink is ultimately limited by the rate of the transfer of carbon, or carbon subduction rate, from the mixed layer to the ocean interior (Carroll et al., 2022; Bopp et al., 2015; Iudicone et al., 2011). Once taken up by the ocean, the carbon is stored in the mixed layer in the form of DIC, where it remains subject to air-sea gas exchange. Only subduction below the mixed layer base can guarantee sustainable sequestration on timescales that could reach decades to centuries (Drake et al., 2018), maintaining the size of

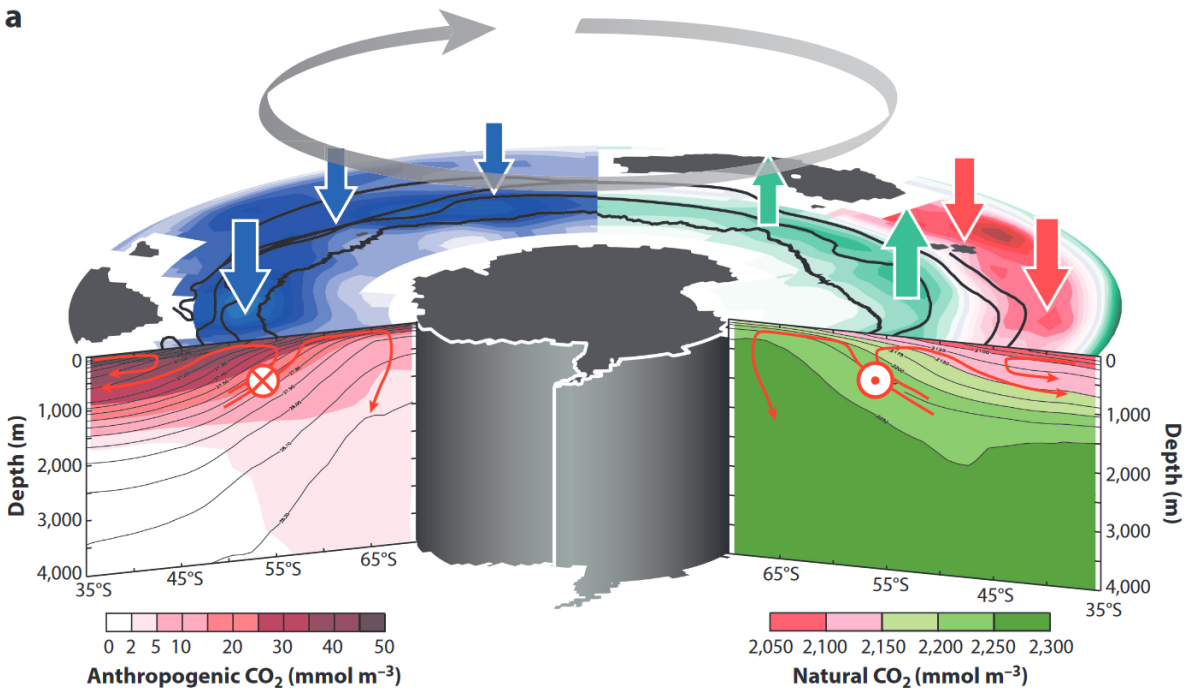

Figure 1.1: Schematic of the anthropogenic (left) and preindustrial (right) carbon content and circulation, adapted from Gruber et al. (2019b). The carbon content is derived from the ocean inversion results described in Gruber et al. (2009).

the oceanic carbon interior pool (Graven et al., 2012). Carbon can also be obducted back in the mixed layer in regions where processes support the upward transfer of carbon-rich waters, and in specific (frontal) regions sometimes shortly after being subducted (Toyama et al., 2017; Sallée et al., 2012). The subduction and obduction of DIC through the mixed layer is called the solubility pump (Fig.1.2). In the euphotic zone, DIC can also be used by autotrophic or mixotrophic organisms - and thereby transformed into dissolved and particulate organic carbon (DOC and POC, respectively) and carbon mass contained inside zooplankton and phytoplankton organisms, or be used by organisms to produce calcareous shells (called here particulate inorganic carbon - PIC) (Boyd et al., 2019). In the following, we regroup all these terms of biologically-induced carbon (with the exception of PIC which accounts for very little in terms of mass fluxes compared to POC, DOC and plankton mass) under the global term of total organic carbon (TOC). For the carbon to be sequestered over long time scales, TOC also needs to be transferred below the mixed layer, and after remineralization can be obducted back into the mixed layer: those two transfers form the biological pump (Fig.1.2).

While the deployment of hundreds of autonomous biogeochemical floats since 2014 has improved the quantification of air-sea fluxes of total carbon dioxide (CO_2) in all seasons

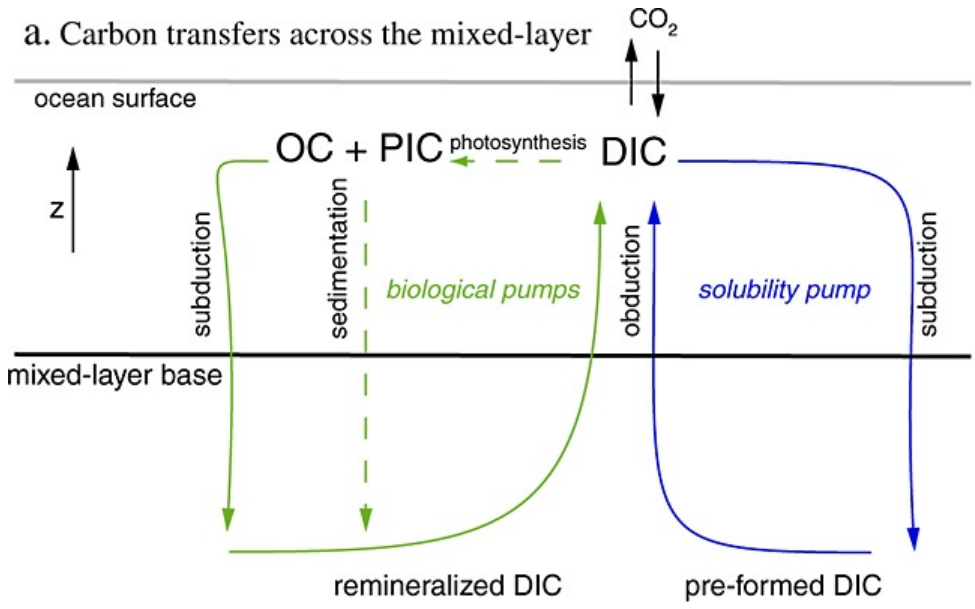

Figure 1.2: Schematic of the biological (left) and solubility (right) pumps of carbon. Taken from Levy et al. (2013).

(Bushinsky et al., 2019; Gray et al., 2018; Williams et al., 2017), carbon subduction rates remain difficult to quantify from observations.

Carbon subduction rates depend on several physical processes which allow the transfer below the mixed layer. Carbon is obducted and subducted at the base of the mixed layer via *physical transfer*. This transfer includes vertical advection (mostly driven by Ekman pumping and suction), horizontal advection across the sloped mixed layer base (sometimes referred to as lateral induction), along-isopycnal diffusion induced by mesoscale eddies and small-scale mixing, vertical diffusion due to turbulent mixing across the mixed layer base, and the seasonal entrainment/detrainment due to the seasonal mixed layer fluctuations (Fig. 1.2, Bopp et al., 2015; Levy et al., 2013). The different processes do not have the same magnitude and role for preindustrial DIC, anthropogenic DIC (and as a consequence for the sum, that is historical DIC) and TOC. In a study using a coarse-resolution model, vertical advection is found to dominate the transfer of preindustrial DIC across the mixed layer base, leading to a net obduction, while obduction by vertical mixing is found to be one order of magnitude smaller (Levy et al., 2013). They find that horizontal advection drives only a small part of preindustrial DIC subduction, and eddy mixing partly counters it. In total, the SO represents 25% of the net obducted preindustrial DIC over the global ocean, as expected from the large upwelling of DIC-rich deep waters: it creates a physical transfer up to the mixed layer, and then back to the atmosphere (Levy et al., 2013). In contrast, a study by

Dufour et al. (2013) find that vertical diffusion dominates over other advective processes for preindustrial DIC obduction. For historical DIC (preindustrial + anthropogenic) subduction, Carroll et al. (2022) show in a study based on a data assimilated model that obduction into the mixed layer is driven by advective and diffusive processes. In the SO, the net diffusive term is slightly higher than the net advective term, result that they attribute to a larger mixing in boundary currents and the formation of water masses. This physical obduction is counterbalanced by a net subduction attributed to the uptake of DIC by organisms to produce organic matter: the latter dominates and results in a net subduction of historical DIC in the Southern hemisphere.The physical transfer of anthropogenic DIC is dominated by vertical mixing (mainly vertical diffusion) in contrast to preindustrial DIC, in two studies using a similar model and configuration as Levy et al. (2013)(Toyama et al., 2017; Bopp et al., 2015). However, observation-based estimates of anthropogenic carbon subduction suggest that the role of vertical diffusion is negligible in regards to that of advection (Sallée et al., 2012). Overall, the relative roles of advection and vertical mixing in DIC physical transfer remain unclear and have only been studied in low-resolution models.

TOC is thought to be mainly transferred via *biological transfer* (gravitational pump, through sedimentation) (Boyd et al., 2019; Levy et al., 2013). However, other mechanisms need to be taken into account to obtain a realistic organic carbon export rate to depth, such as the physical transfer (same processes as for DIC), or the migrant pump e.g. the vertical migration of organisms (Boyd et al., 2019). These other mechanisms are generally not accounted for in observation-based studies (e.g., Giering et al., 2023), whereas physical transfer of TOC below the mixed layer has been shown to account for more than half of the gravitational pump in a non-eddy-permitting model (Levy et al., 2013). In the model, the physical transfer is mainly driven by vertical mixing, due to the strong gradient of organic carbon at the base of the mixed layer and seasonal entrainment below the mixed layer in winter (Levy et al., 2013). Observations also show that physical transfer is important and maximized in regions of high productivity (Stukel and Ducklow, 2017).

Physical processes for the carbon subduction rate show high spatial variations across the SO. Bopp et al. (2015) and Sallée et al. (2012) find that the spatial variability of the total subduction of anthropogenic carbon is dominated by advective fluxes. A similar result has been obtained for preindustrial DIC (Levy et al., 2013). Sallée et al. (2012) specify that these advective flux patterns mainly correspond to hotspots of reventilation and subduction, located next to each other, in specific regions where the mixed layer is sloped in regard to the mean flow. Therefore, downward and upward advective fluxes partly compensate at a local scale, such that integrated over the whole region, the total (horizontal and vertical) advective component of the subduction fluxes becomes small. In contrast, vertical mixing is

always directed downwards and therefore becomes the major subduction pathway in model simulations, when integrated over the SO (<44°S) (Bopp et al., 2015). Advective fluxes are also countered by the eddy-induced subduction in both models (Levy et al., 2013; Bopp et al., 2015) and observational estimates (Sallée et al., 2012). For historical DIC, hotspots of diffusive fluxes appear in western boundary currents, where some warm and cold water masses mix (Carroll et al., 2022).

Resolving or not mesoscale eddies in ocean models leads to large differences in the circulation, such as the pathways and time scales of deep water upwelling, especially in the SO where the strong ACC spawns a vigorous eddy field (e.g., Drake et al., 2018; Tamsitt et al., 2017; Dufour et al., 2012; Marshall and Speer, 2012; Hallberg and Gnanadesikan, 2006). In the SO, eddy transport oppose the wind-driven circulation and contribute to restratify the water column which is also expected to play a role in anthropogenic carbon subduction (Sallée et al., 2012). The advection of tracers by the mean circulation is strongly compensated by eddy-driven advection, thus reducing the transport of preindustrial DIC towards the surface Dufour et al. (2013). Eddies can also enhance the transfer of tracers from and to the ocean interior in localized regions (Brady et al., 2021; Balwada et al., 2018), and increasing the resolution enhances the eddy saturation/compensation taking place in the SO (Adcroft et al., 2019; Morrison and McC. Hogg, 2013; Dufour et al., 2012; Farneti et al., 2010).

While eddying ocean models explicitly resolve (at least to some extent) the impact of mesoscale eddies on the circulation of DIC at the base of the mixed layer, non-eddying models, such as the ones used in Toyama et al. (2017); Bopp et al. (2015); Levy et al. (2013), need to parameterize the transport (bolus transport) and isoneutral diffusion driven by mesoscale eddies. Previous studies have shown that eddy-permitting models give better estimates of oceanic storage of anthropogenic DIC than their lower resolution counterparts (Terhaar et al., 2019; Lachkar et al., 2007). Whether this better representation of storage arises from the more accurate representation of subduction at the base of the mixed layer or from a more accurate redistribution of carbon in the ocean interior by the circulation is yet to be determined and addressing this question will require refined measurements of subduction rates. In addition to impacting the magnitude and patterns of subduction fluxes, an increased resolution is likely to impact the respective roles of physical processes in transferring carbon to the ocean interior.

In this study, we investigate the processes that drive the transfer of organic and inorganic carbon across the base of the mixed layer in the SO. To do so, we use an eddy-permitting global ocean model run under preindustrial and historical scenarios allowing us to separate the preindustrial and anthropogenic carbon components. The contribution of physical processes to the physical and biological transfer of carbon across the mixed layer base is

examined in distinct dynamical regions of the SO. For organic carbon, we also compare the relative roles of physical and biological transfers.

Chapter 2

Methods

2.1 Model configuration and simulations

2.1.1 The NEMO -PISCES model in the eORCA025 global configuration

We use the NEMO (Nucleus for European Modelling of the Ocean) model platform, which comprises the ocean general circulation model "Océan Parallélisé" (OPA - Parallelized Ocean in English) developed by Madec et al. (1998). OPA runs with a nonlinear equation of state and a series of approximations, including the Boussinesq and hydrostatic approximations (Madec, 2008). The ocean component is coupled with the thermodynamical and dynamical Louvain-la-Neuve sea Ice Model (LIM3) (Vancoppenolle et al., 2009), to give the heat, salinity and momentum fluxes at the sea-ice boundaries. LIM3 is divided in five ice categories, which are themselves divided in six layers: 1 layer of snow and 5 layers of ice. Each category has its own properties, such as salinity, age, volume, enthalpy (Vancoppenolle et al., 2009). The biogeochemical component of the ocean model is the Pelagic Interaction Scheme for Carbon and Ecosystem Studies (PISCES) biogeochemical model (Aumont et al., 2015) which holds 24 prognostic tracers (Fig.2.1). PISCES includes four prognostic carbon variables, which are DIC, DOC, POC (divided in two class sizes of big particles of high sinking speed and small particles of low sinking speed) and PIC (similar decomposition as POC). The DIC concentration is computed following the Ocean Carbon-Cycle Model Intercomparison Project protocols (Orr et al., 2017). It consists of the sum of the concentrations of the different dissolved forms of CO_2 (DIC=$HCO^-_{3(aq)} + CO^{2-}_{3(aq)} + CO_{2(aq)}$). There are two zooplankton size classes with carbon content (microzooplankton and mesozooplankton) and two phytoplankton compartments with carbon content (diatoms and nanophytoplankton). The plankton biomasses (expressed in carbon), the POC and the DOC can be combined into

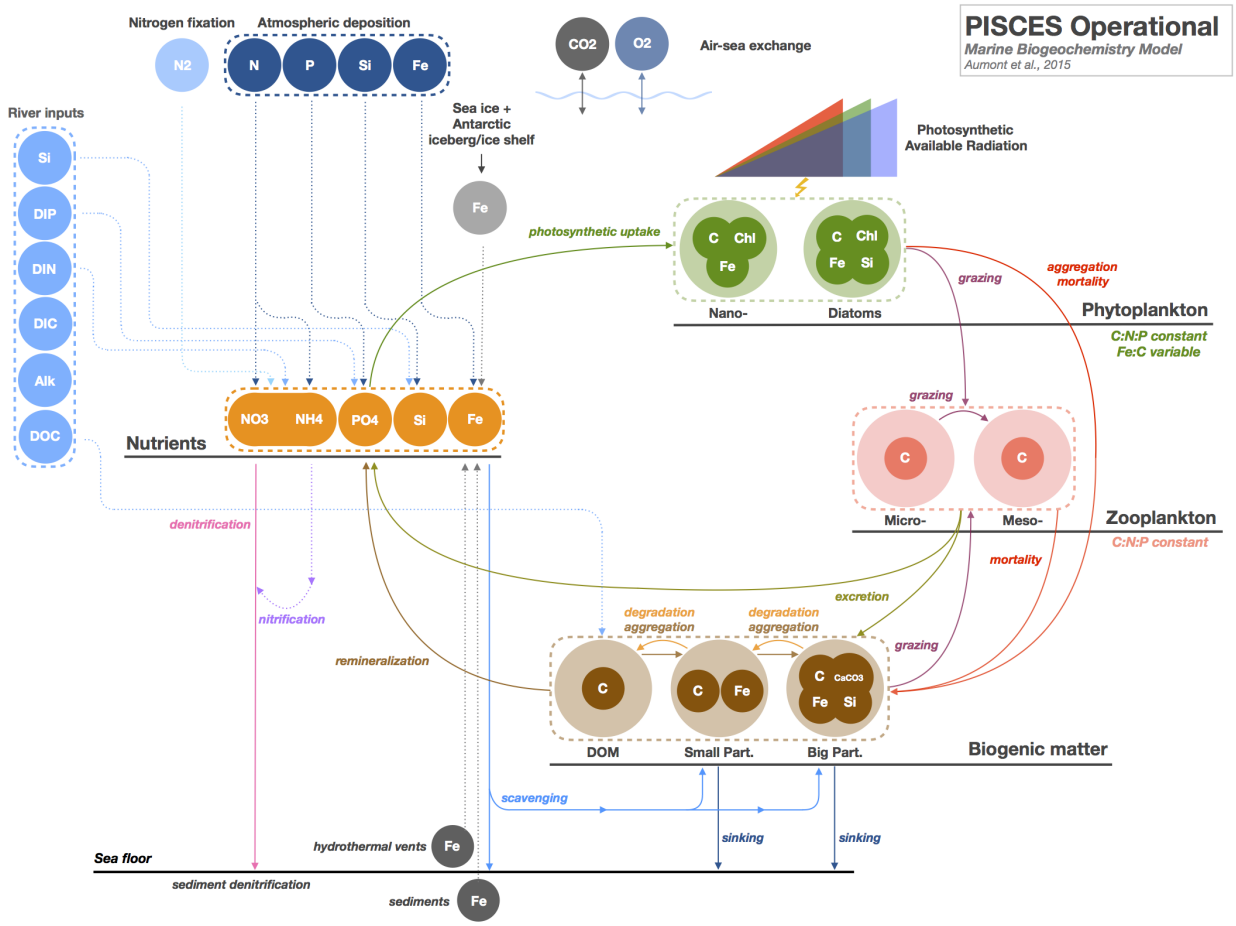

Figure 2.1: "Schematic diagram of the standard "Operational" version of PISCES describing the nutrients, carbon and oxygen cycles and processes modeled." Reproduced from https://www.pisces-community.org/index.php/model-description/

the TOC. PISCES also includes dissolved oxygen, alkalinity, and five nutrients (phosphate (PO_4), ammonium (NH_4), nitrate (NO_3), silicium (Si) and iron (Fe)). The phytoplankton growth depends on the availability of nutrients and the nutrient Redfield stoechiometric ratio are kept constant (Aumont et al., 2015).

CO_2 air-sea fluxes are computed within the model following Wanninkhof (1992):

$$F_{CO_2} = (1 - ice) \times K(pCO_2^{atm} - pCO_2^{ocean}) \tag{2.1}$$

with K the gas transfer velocity depending mainly on the temperature and the wind speed, pCO_2 the partial pressure of CO_2 in the ocean (pCO_2^{ocean}) and the atmosphere (pCO_2^{atm}), and *ice* the sea ice total fraction. The CO_2 partial pressures of the ocean and the atmosphere tend to equilibrate themselves (with a time lag of around 6 months) through air-sea carbon fluxes.

The model is run in the eORCA025 configuration, which has a nominal resolution of 0.25° at the Equator for both latitude and longitude and uses a tripolar grid with a global orthogonal curvilinear ocean mesh applied to a Mercator projection resulting in grid sizes of around 17 km at 50°S and 5.6 km (zonal direction) and 3.2 km (meridional direction) at the highest latitudes (Madec and Imbard, 1996). The horizontal grid is refined near the Antarctica shelf in order to represent more accurately the Antarctic under-ice shelf seas contribution to the SO freshwater cycle (Mathiot et al., 2017). In the vertical, the water column is split in 75 levels with grid thickness increasing with depth from 1 m at the surface to around 200 m at the bottom. The 0.25° resolution allows for the partial resolution of mesoscale eddies (Hallberg, 2013). Here, the parameterizations of Gent and McWilliams (1990) andRedi (1982) are used with coefficients of 300 $m^2.s^{-1}$ and 100 $m^2.s^{-1}$, respectively, to obtain physical and biogeochemical fields that remain close to observations while allowing for some explicit representation of mesoscale eddies. In coarser resolution configurations, those coefficients are typically set to much larger values: for example, both coefficients are set to 2000 $m^2.s^{-1}$ in ORCA2, the 2° resolution counterpart of ORCA025 (Bopp et al., 2015).

2.1.2 Preindustrial and historical simulations

Two simulations are run: one with preindustrial carbon forcing (PIND) and one with historical carbon forcing (HIST), following the Global Carbon Budget protocol (Hauck et al., 2020). In PIND, the atmospheric CO_2 concentration corresponding to 1850 (278 ppm) is kept constant throughout the simulation. PIND is initialized from GLODAPv2 preindustrial DIC field Olsen et al. (2016). The atmospheric CO_2 concentration in HIST follows the Global Carbon Budget time series Friedlingstein et al. (2020). HIST is initialized with GLODAPv2 historical DIC concentrations computed by adding to the preindustrial DIC field the anthropogenic DIC field in 1958 of an ORCA05 simulation from Terhaar et al. (2019). Both simulations are run from 1958 to 2014 using the atmospheric fields from the Drakkar forcing set 5 version 2 (DFS5) Dussin et al. (2016). Subtracting PIND from HIST gives the anthropogenic component of carbon in the ocean. As the circulation is the same between PIND and HIST, this approach allows to investigate the passive penetration of anthropogenic carbon into the ocean (which is obtained with climate models after decomposition between the passive penetration and the effect of changes in the circulation Chen et al. (2019)).

2.1.3 Observational products

We use the data-based product from Gray et al. (2018) to evaluate air-sea CO_2 fluxes

in our HIST simulation. This product is derived from measurements taken by BGC-Argo floats until the end of 2020 in the SO by the Southern Ocean Carbon and Climate Observations and Modeling (SOCCOM) program. Fluxes are reconstructed based on measured pH, temperature, salinity and estimated alkalinity (Gray et al., 2018), following the formula from Wanninkhof (1992). We also use Bushinsky et al. (2019)'s product that combines the BGC-Argo float reconstructed fluxes of Gray et al. (2018) taken from 2015 to 2017 and the climatology of Landschützer et al. (2020) from 1987 to 2014, interpolated on 2015-2017. This climatology is based on the Surface Ocean CO_2 Atlas (SOCAT) dataset and uses a neural network method to reconstruct pCO_2 from other environmental variables (Landschützer et al., 2013).

We compare the observation-based products of GLODAPv2 to our historical and anthropogenic carbon storage. DIC content is gravimetric in this dataset, while it is volumetric in our model. Therefore, we convert the mol/kg into mol/m^3 by multiplying by the constant in situ density of 1028 kg/m^3 used in NEMO.

Mixed layer observations come from the dataset described in Hosoda et al. (2010), with observations from Argo floats profiles taken from 2001 to 2015.

To evaluate the salinity and the potential temperature in the model (and hence the potential density), we use the data from the CORA5.2 dataset (Szekely et al., 2019), based on Argo floats measurements combined with CTD casts from several programs and the World Ocean Database 2013 (WOA13) (Locarnini et al., 2013; Zweng et al., 2013).

2.2 Analyses

2.2.1 Southern Ocean regions

In order to compare the modelled air-sea CO_2 fluxes to observational estimates, we use the five Southern Ocean regions defined in Gray et al. (2018) for all our analyses. Each region corresponds to a different dynamical and biogeochemical province of the Southern Ocean south of 35°S and each boundary is averaged over 1995-2014. The boundaries of the regions are defined using the dynamical and biogeochemical characteristics of our model to ensure consistency with the model solution. The five regions and the definition of our boundaries are represented in Fig.2.2. From south to north, we have:

- **The Sea Ice Zone (SIZ)** is defined as the region where the September sea ice concentration is greather than 15% (Sea Ice Front - SIF).
- **The Antarctic Southern Zone (ASZ)** is located between the SIZ and the Polar Front (PF). The PF is defined as the sea surface height (SSH) contour located at

the local maximum of SSH meridional gradient within a [-0.5°,+2°] band around the 2°C isotherm latitudinal maximum between 50 m and 300 m. This isotherm maximum corresponds to the northernmost extension of the Antarctic Winter Waters (Park et al., 1998). The SSH contour of the PF is computed as the average of 10 SSH contours each defined at different longitudinal sections across the SO following Dufour et al. (2015).

- **The Polar Frontal Zone (PFZ)** is located between the PF and the Subantartic Front (SAF). The SAF is defined as the SSH contour located at the local maximum of SSH meridional gradient in a varying band from 1° to 10° depending on the longitudinal section south of the winter mixed layer depth maximum found north of the ACC. The SSH contour of the SAF is computed as the average of 8 SSH contours each defined at different longitudinal sections across the SO, similarly to the PF.

- **The Subantarctic Zone (SAZ)** is defined north of the SAF and south of the Subtropical Front (STF) which corresponds to the location of the 11°C isotherm of conservative temperature at 100 m (Orsi et al., 1995).

- **The Subtropical Zone (STZ)** is defined north of the STF and south of 35°S.

Table 2.1 summarizes the surface area of each region, and compares them to areas of the regions of Gray et al. (2018). Our total area is larger than that of Gray et al. (2018), which is due to difference in coastal resolution. This difference in coastal resolution also partially explains the larger SIZ and STZ that we obtain. While our ASZ is larger than our PFZ, it is the contrary in the observations due to our different definitions of the PF and the SAF.

Table 2.1: Areas of the five regions of the SO in 10^7 km^2, represented in figure 2.2

	SIZ	ASZ	PFZ	SAZ	STZ	Total
Our model	2.03	1.47	1.25	2.03	2.49	9.27
Gray et al. (2018)	1.72	1.28	1.43	1.94	2.26	8.64

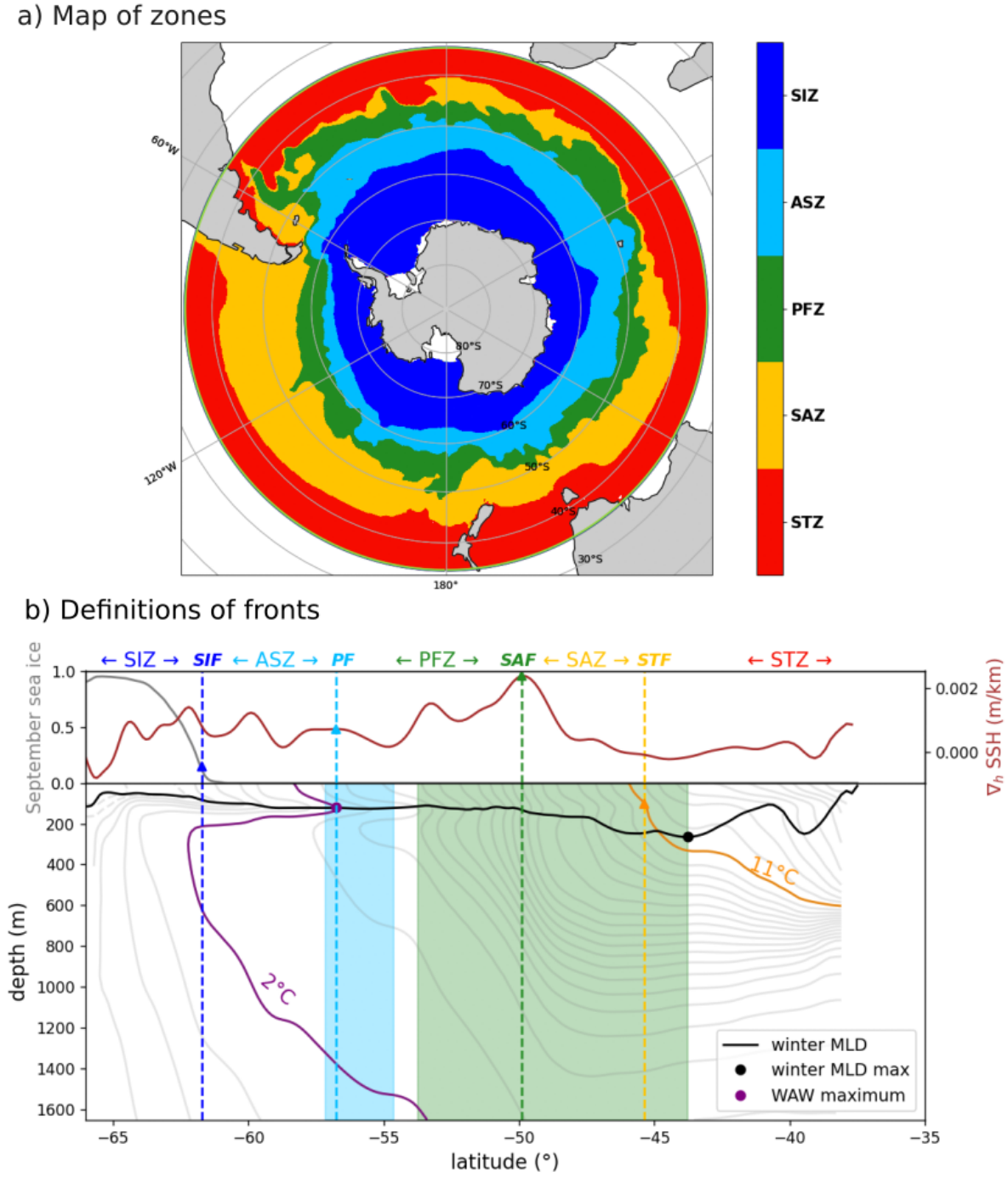

(Caption on next page.)

Figure 2.2: a) The five dynamic regions of the Southern Ocean used in the study. From South to North: Sea Ice Zone (SIZ), Antarctic Southern Zone (ASZ), Polar Frontal Zone (PFZ), Subantarctic Zone (SAZ), and Subtropical Zone (STZ). b) Example of the boundary detection procedure for a meridional section at 140°E (one of the sections we use). The SIF, PF, SAF and STF are represented in dotted lines. In the upper plot, the September sea ice fraction is represented in grey, with the triangle at 0.15 marking where we define our SIF. The potential temperature is contoured in the background of our lower plot and the 2°C isotherm is highlighted in purple, for the Antarctic Winter Waters (AWW) maximum. A [-0.5°,2°] band is highlighted in blue, in which we search for the local maximum of the SSH meridional gradient, represented in brown in the upper plot. The maximum of SSH gradient (location of the PF) is marked by the blue triangle. The winter MLD is represented in black in the lower plot and shows a maximum north of the ACC. A 10° latitudinal band south of this maximum is highlighted in green, where we take again the local maximum of the SSH meridional gradient as our SAF definition (green triangle in the upper plot). Finally, we represent in orange the 11°C isotherm and show with an orange triangle its intersection with the 100 m depth, which is our definition of our STF.

2.2.2 Computation of subduction fluxes

The subduction fluxes of DIC and TOC are computed online at every time step across the time-varying mixed layer base and then combined using the method described in Karleskind et al. (2011),Levy et al. (2013) and Bopp et al. (2015):

$$F_{C,sub} = \int_t \underbrace{-C_h(w_h + \boldsymbol{u}_h.\boldsymbol{\nabla} h) + F_{C,GM}}_{\text{total advection}} + \underbrace{k_z^h.\partial_z C_h}_{\text{vertical diffusion}} + \underbrace{-C_h.\partial_t h}_{\text{temporal entrainment}} + \underbrace{F_{C,Redi}}_{\substack{\text{Parameterized} \\ \text{isopycnal diffusion}}} \quad dt \tag{2.2}$$

The first term on the right hand side is the total (vertical and horizontal) advection of tracer C through the base of the mixed layer, where C_h is the concentration of DIC or TOC, w_h is the vertical velocity, $\mathbf{u}_h$ the horizontal velocity at the base of the mixed layer (subscript h) and $F_{C,GM}$ the subduction by the parameterized eddy driven transport (Gent et al., 1995). The advection in $F_{C,GM}$ represents only around 5% of the total advection given that the coefficient used is relatively small (see Section 2.1). For this reason, we do not separate the parameterized term from the non-parameterized term for advection. The second term in brackets corresponds to the vertical diffusion of tracer C across the mixed layer base with k_z^h the vertical diffusion coefficient and $\partial_z C_h$ the vertical gradient of C across the base of the mixed layer. Vertical diffusion coefficients k_z^h are derived from the Turbulent Kinetic Energy (TKE) closure scheme of Blanke and Delecluse (1993) with improvements from Madec (2008) and vary around the value of 1.2 10^{-5} m^2 s^{-1}. The third term is the entrainment/detrainment of C due to the temporal variations of the mixed layer depth h.

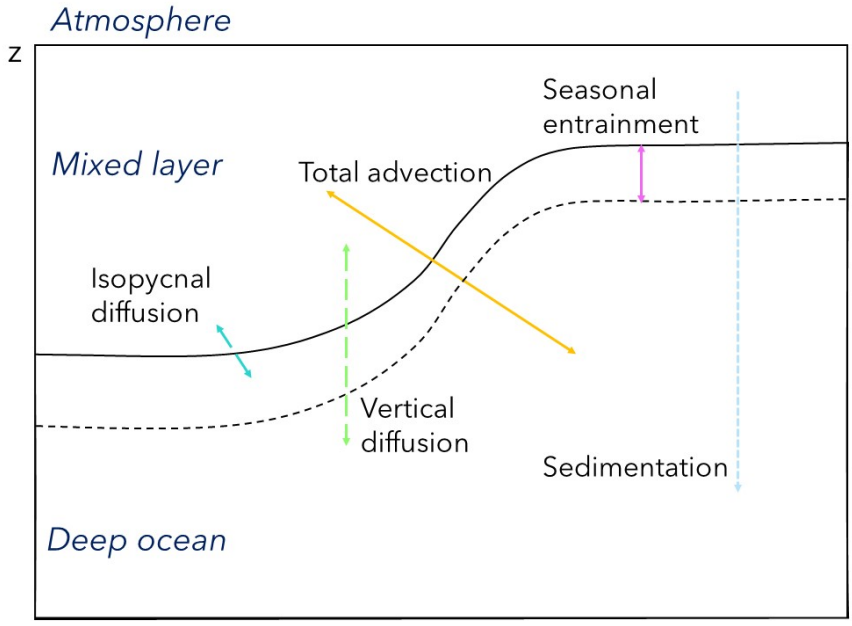

Figure 2.3: Decomposition of fluxes at the mixed layer base. Schematic adapted from Levy et al. (2013).

The term $F_{C,Redi}$ corresponds to the along-isopycnal diffusion (Redi, 1982).

In the model, the biological transfer of carbon is achieved solely by the gravitational pump, i.e. the sedimentation of organic carbon particles, computed as the sinking rate of particles and organisms containing carbon across the mixed layer. Other processes such as the mesopelagic-migrant pump or the seasonal lipid pump are not included (Boyd et al., 2019). The total decomposition is summarized in Fig.2.3.

The addition of carbon to the atmosphere leads to a pH increase that impacts the biological processes affecting in turn the TOC concentration, the TOC subduction and the gravitational pump. As this impact is small overall, it is neglected in our analysis, resulting in biological transfer and physical transfer rates being identical in both our historical and preindustrial simulations.

2.2.3 Budgets in the mixed layer

Carbon budgets in the mixed layer are computed offline for each of our five regions. For DIC and TOC, the budget is computed respectively as (with fluxes oriented upward):

$$\frac{\partial DIC_{hist}}{\partial t} = -F_{DIC,air-sea} + F_{DIC,sub} - \nabla_h F_{DIC,bound} - F_{DIC,bio} + Residual \qquad (2.3)$$

$$\frac{\partial TOC}{\partial t} = +F_{TOC,sub} - \nabla_h F_{TOC,bound} + F_{TOC,bio} + F_{TOC,grav} + Residual \qquad (2.4)$$

with $\frac{\partial DIC_{hist}}{\partial t}$ the DIC tendency term in the mixed layer, $F_{DIC,air-sea}$ the sea-air fluxes, $F_{C,sub}$ the upward subduction fluxes at the mixed layer base, $\nabla_h F_{C,bound}$ the horizontal divergence of fluxes across the region boundaries, $F_{C,bio}$ the rate at which inorganic carbon is transferred to organic carbon and $F_{TOC,grav}$ the gravitational pump. Horizontal fluxes of our carbon tracers are computed at each boundary using monthly averaged horizontal velocities and tracer concentration, except for anthropogenic carbon for which they are computed as the residual of the budget. The residual for all tracers includes errors resulting from the computation of horizontal fluxes at a monthly frequency (whereas other terms are computed at each time step), and other budget terms including river runoff and horizontal diffusion that are not accounted for here due to the lack of the corresponding model output. The budget for anthropogenic DIC is computed in a similar way as in Eq. 2.3 with the exception of the term $F_{DIC,bio}$, as it is identical for both historical and preindustrial DIC and therefore disappears when they are subtracted to obtain anthropogenic DIC.

All our results are presented averaged over the period 1995-2014 (the last twenty years of our simulations).

2.3 Evaluation of the simulations

2.3.1 Mixed layer depth

In the model, the spatial distribution of the mixed layer depth is overall similar to that of the observations (Fig. 2.4). In particular, deep MLD patterns in the East Pacific and Indian sectors are well represented, with a moderate downstream (eastward) shift of the deepest MLD compared to observations. However, the maxima found in the model MLD south of the South African coast in the STZ does not appear in observations. We find that in summer (January), mixed layer depth (MLD) is shallower than in the observations by 14 m on average between 35°S and 70°S. In winter (August), our mixed layer is on average shallower by 19 m. This shallower bias likely comes from a lack of wind energy input in our model or from the vertical mixing parameterization scheme that does not account for some wind effects (e.g., swells, near-inertial oscillations) (Rodgers et al., 2014). We can note that deep bias is generally found in non-eddying and eddy-permitting models in winter due to the lack of restratification by mesoscale eddies. Refining the horizontal resolution or adding a mesoscale eddy transport parameterization both act in reducing this bias Adcroft et al. (2019). Running our model with both parameterization and eddy-permitting resolution might be the

reason for the absence of this bias.

2.3.2 Air-sea CO_2 fluxes

Over 2009-2014, our air-sea CO_2 fluxes attain -1.13±0.04 PgC/year on average south of 35°S, corresponding to an uptake of 0.17±0.03 PgC/year of preindustrial carbon and of 0.96±0.06 PgC/year of anthropogenic carbon (see Fig.2.5). Our model takes up historical carbon in all regions of the Southern Ocean, including south of the ACC, in contrast to observations from Argo (Gray et al., 2018, SOCCOM) that show an outgassing both in the SIZ and ASZ, and to combined ship and Argo floats observations (Bushinsky et al., 2019, SOCCOM+SOCAT) that show an outgassing in the ASZ. Our model fluxes are in better agreement with the SOCAT dataset, with similar uptake in all regions. The SOCCOM data show a much smaller uptake than the SOCAT data in the PFZ, the SAZ and the STZ, our model results being between those two estimates. A caveat on the comparison with observational datasets is that we use the time period 2009-2014, while the SOCCOM data span over the period 2014-2020 and SOCAT data begin in 1982. Moreover, the data used in Bushinsky et al. (2019) only span 2015-2017. The new observations from SOCCOM (Gray et al., 2018) are the first ones showing an outgassing south of the ACC while most ocean models and SOCAT data show an uptake. This important difference between SOCCOM estimates and other estimates has been attributed to year-round measurements that autonomous floats allow. SOCCOM CO_2 flux estimates show a strong outgassing in the winter that would go undetected by other datasets. However, uncertainties persist on this signal as observations do not span a large period and CO2 fluxes are nort directly measured.

Model air-sea fluxes show a continuous increase of CO_2 uptake from the SIZ to the STZ (Fig.2.6). Across basins, we find higher air-sea fluxes in the Atlantic and Indian Ocean compared to the Pacific Ocean, which are likely to follow the patterns of partial pressure of CO_2 at the sea surface (Landschützer et al., 2020). We also note small regions of outgassing in the ASZ, south of Australia (Fig.2.6). In the STZ, where the strongest fluxes are found, we find maxima in western boundary currents such as the Agulhas Current and the East Australian Current.

The seasonal climatology of our air-sea CO_2 fluxes over 1995-2014 do not correspond to recent observational-based products (Fig. 2.7). While Gray et al. (2018); Bushinsky et al. (2019) observed a strong outgassing of CO_2 in winter, mostly in the ASZ but also in the PFZ, the SIZ and the SAZ, our model shows a stronger uptake in winter and spring in all regions except for the SIZ. This opposite phase in the seasonal cycle of air-sea CO_2 fluxes between

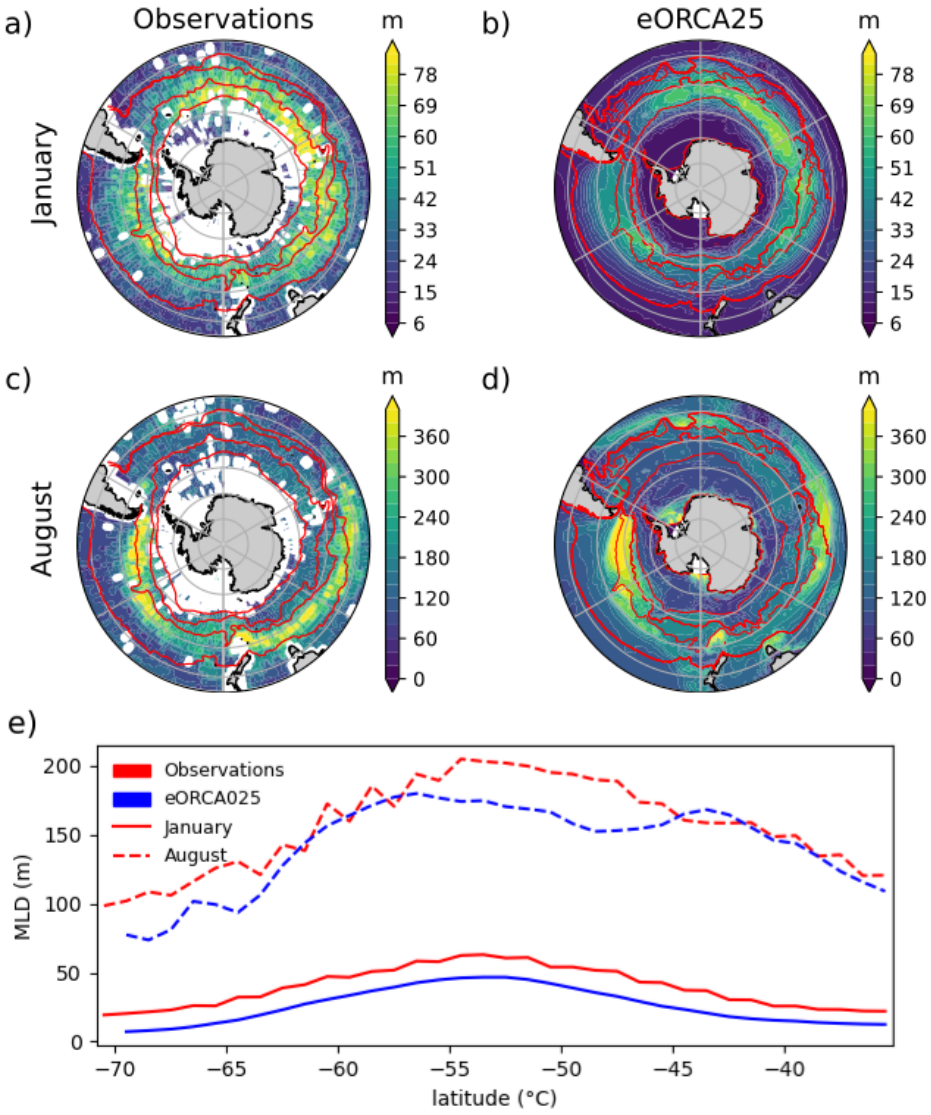

Figure 2.4: MLD for (a,b) January (month of the shallowest mixed layer) and (c,d) August (month of the deepest mixed layer) averaged over the period 1995-2014 (our model) and 2001-2015 (observations). This time period is the best overlap between the observational dataset and simulation time periods. Observations (a and c) are from Hosoda et al. (2010) and are based on Argo float measurements using the density criterion of $\Delta\sigma = 0.03$ kg.m^{-3} following (de Boyer Montégut, 2004). e) shows the meridional average in our model and the observations, for both January and August.

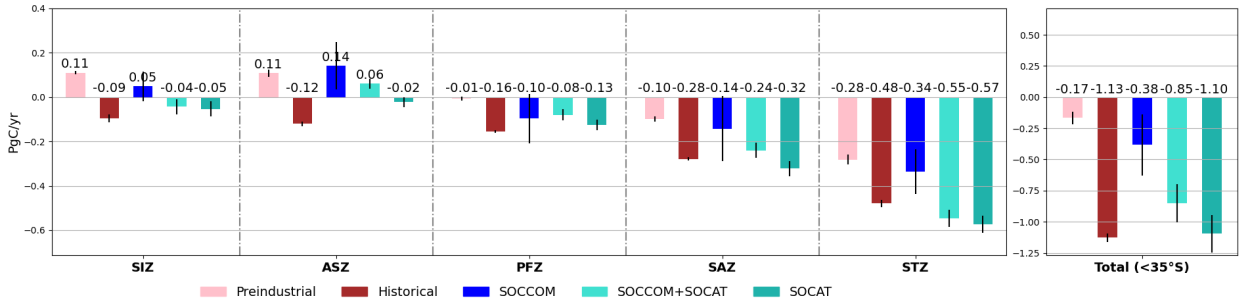

Figure 2.5: Regional integration of preindustrial and historical air-sea fluxes from our model, and comparison with air-sea fluxes from SOCCOM BGC-Argo (Gray et al., 2018) and combination of SOCCOM and SOCAT datasets by Bushinsky et al. (2019) Positive fluxes correspond to outgassing. Model fluxes are integrated between 2009 and 2014, while observations were taken from 2014 to 2020 for Gray et al. (2018), and interpolated on 2015-2017 for SOCAT + SOCCOM and SOCAT only (Bushinsky et al., 2019). Error bars correspond to interannual variability in our model, and are obtained with en emsemble of Monte Carlo simulations for observations (Gray et al., 2018) and as the standard deviation in Bushinsky et al. (2019).

models and observations has been highlighted in many models. Mongwe et al. (2018) propose that while model seasonality is dominated by strong sea surface temperature variations, leading to an enhanced solubility in winter, observations show a domination from the rate of change of the DIC concentration at the surface, due to a weaker stratification (so deeper MLD - see analysis below) in the observations (see Fig.2.8.c,f) which allows more DIC obduction to the surface, and a change in the intensity and the duration of the phytoplankton bloom.

2.3.3 DIC fields

Our model shows a smaller historical DIC content within the DIC-rich CDW compared to observations (Fig.2.8.a-b), with a maximum difference at around 230 m depth. This difference results from a higher stratification and less outcrop of deep waters in our model (Fig.2.8.c) than in observations (Fig.2.8.f). Around 50°S-60°S, the formation of AAIW, following freshening by sea ice melting at the sea surface, dilutes the DIC content south of the PF (between around 2150 and 2200 mmol m^{-3}), with a salinity minimum at depth of 34.4 - 34.6 psu represented in Fig.2.8.c,f and in Fig.S1). AAIW are less rich in DIC in our model near the surface (at around 200 m) but richer at depth (around 1000 m) than in observations, probably due to enhance stratification. SAMW (defined by density between 1026.5 and 1027.1 kg.m^{-3}, Li et al., 2021) is the water mass with the most accurate DIC

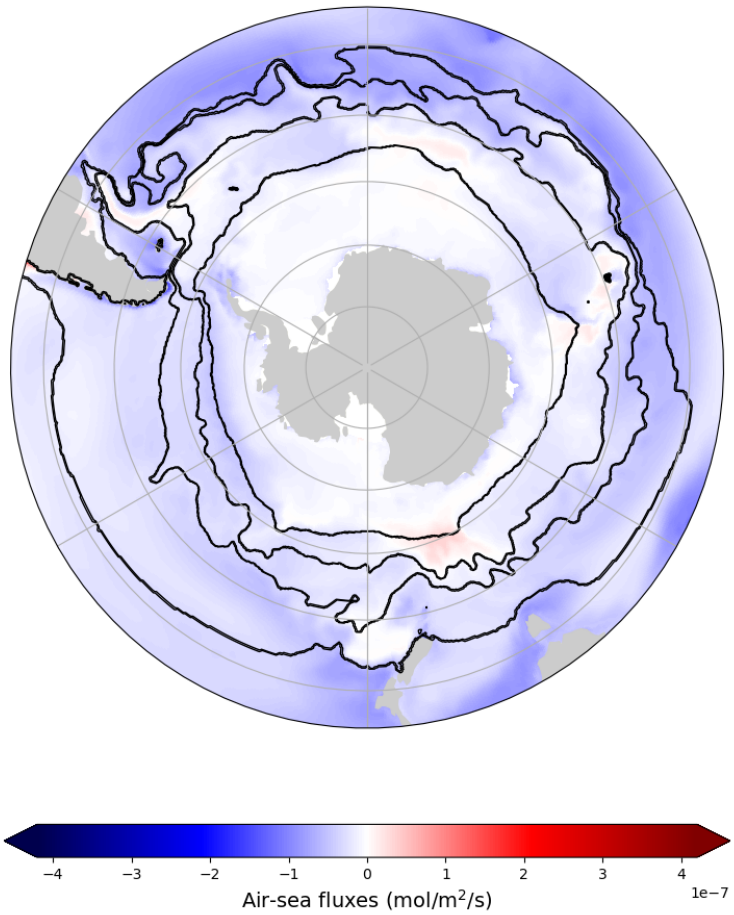

Figure 2.6: Map of historical air-sea CO_2 fluxes averaged over 1995-2014. Contours represent the different boundaries of our regions.

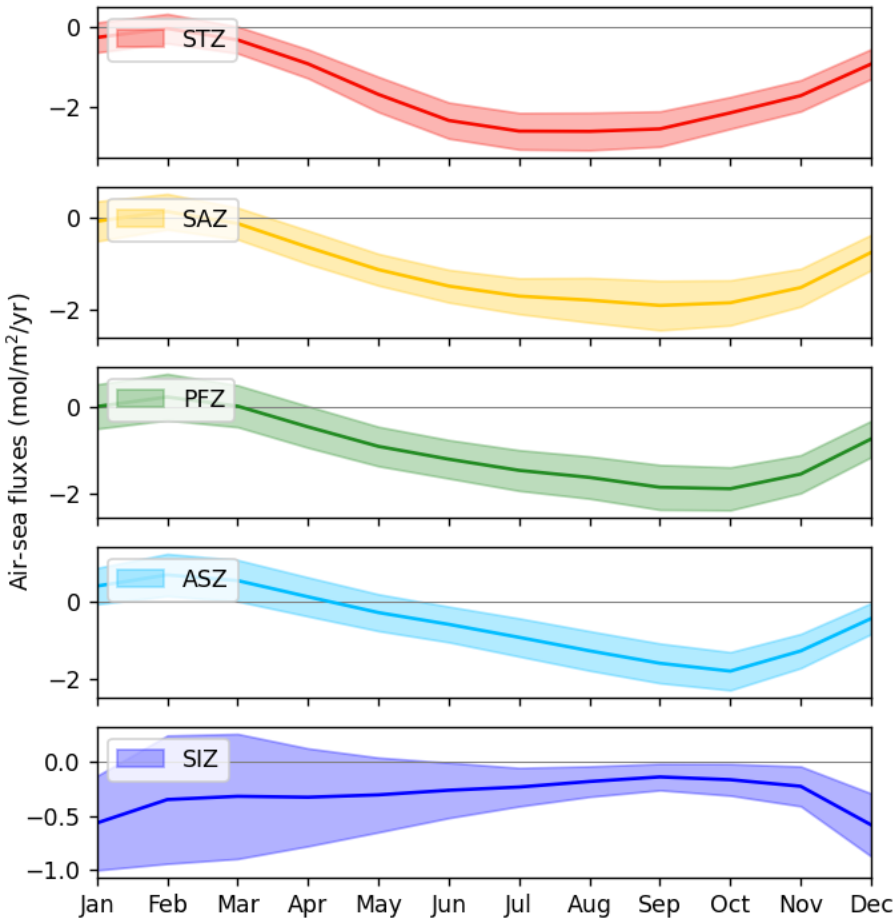

Figure 2.7: Seasonal climatology of air-sea CO_2 fluxes (mol/m^2/s) in our five regions of the SO. The shaded area corresponds to the interannual variability over 1995-2014 for each month. Positive fluxes correspond to outgassing.

concentration, with a difference of only ∼-6 mmol.m^{-3}. Finally, Subtropical Waters have the lowest DIC concentration (below 2100 mmol.m^{-3}) and show a large low bias in our model around 150 m, due to a larger penetration of the DIC-poor STW at depth in the STZ compared to observations.

Anthropogenic carbon concentrations show high values in the STW, with concentrations lowering towards the south and the deep ocean. The model shows a generally low bias, except at the mixed layer depth at 35°S. The bias is strongest in the UCDW and the AAIW, with a maximum in between 400 m and 900 m in the PFZ, corresponding to a shallower penetration of AAIW and SAMW into the interior. This lessened penetration occurs despite a higher salinity at the surface (Fig.S1), whereas Terhaar et al. (2021) have shown that a high salinity between the PF and the STF lead to the formation of denser surface water (AAIW) and hence to more anthropogenic carbon uptake in this region. However, Fig.2.8.c,f shows that this lessened penetration might be due to a higher stratification in this region. Another possibility is the omission of the anthropogenic carbon emitted before 1870 (date of our initialization). Model and observations are closest at the mixed layer in the STZ, where a lack of preindustrial DIC appears to be compensated by more anthropogenic DIC-rich STW.

Overall, both the historical and anthropogenic carbon content are lower in the model in the first 1500 meters below the surface than in the observations-based estimates, presumably due to a higher stratification in our model (as seen with the potential density but also the mixed layer depth in figure 2.8.c,f and Fig.2.4, respectively). However, at the surface in all zones, DIC content is in contrast higher in the model than in the observations. This high bias at the surface could result from the anomalously high uptake of CO_2 present in our model but not in observations (Fig.2.5).

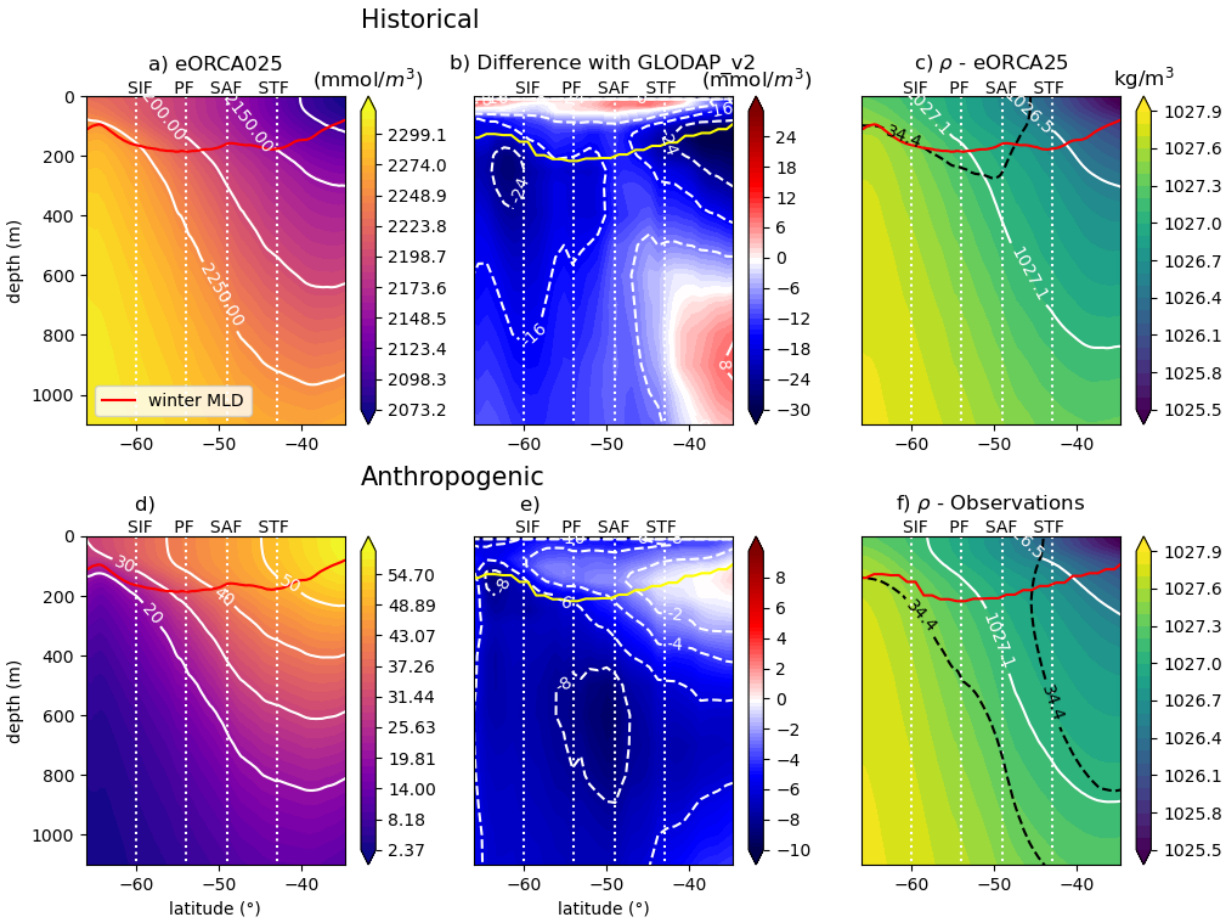

Figure 2.8: Zonally averaged cross-section for (a) historical and (d) anthropogenic DIC in our model, and (b,e) difference (model - observations) with the observation-based GLODAPv2 (Lauvset et al., 2016). Potential density in (c) our model and (f) derived from in situ T and S observations from (Szekely et al., 2019), averaged on 1995-2014 respectively. Black dotted lines correspond to the salinity (PSU) to help locate the AAIW. Red or yellow lines correspond to the mixed layer in model (a,d,c) and observations (b,e,f) from Hosoda et al. (2010).

Chapter 3

Results - Quantification of subduction fluxes across the mixed layer base

3.1 Historical Dissolved Inorganic Carbon

In the SO, historical DIC (DIC_{hist}) is found to be obducted at a rate of 11.2 PgC/year across the base of the mixed layer (Fig.3.1). This rate results from the balance between a large obduction of 21.6 PgC/year south of the SAF, and a weaker subduction of 10.4 PgC/year north of the SAF. This flux pattern is consistent with the general known circulation of water masses circulation in the SO (Gruber et al., 2019b; DeVries et al., 2017). Once obducted in the SIZ, the ASZ and to a lesser extent in the PFZ, historical DIC is transported northward successively through the PF, the SAF and the STF, reaching the PFZ, then the SAZ and the STZ, respectively (Fig.3.1.a). Within the SO, almost half of the DIC_{hist} transported north of the SAF is subducted across the mixed layer base. The other half is transported out of the SO north of 35°S (6.5 PgC/year) or stays as a residual (in part consumed by the biology) in about equal proportions (6.2 PgC/year). Our DIC_{hist} budget shows major residuals in the SAZ and the STZ (Fig.3.1.a). The part resulting from DIC conversion into OC should be approximately the opposite of the residual in the TOC budget (Fig.3.7). However, there are large differences especially in the ASZ, PFZ and SAZ, that we can attribute mostly to uncertainties linked with the computation of meridional transport across the boundaries of our five regions (the DIC tendency term being very small).

Air-sea fluxes are very small compared to the DIC_{hist} fluxes within and at the base of the mixed layer, but nonetheless provide a small contribution in the northernmost regions, with strong fluxes in western boundary currents and in the subtropical Atlantic Ocean in general (Fig.2.6). Overall, even though large amounts of DIC_{hist} are brought back to the mixed layer

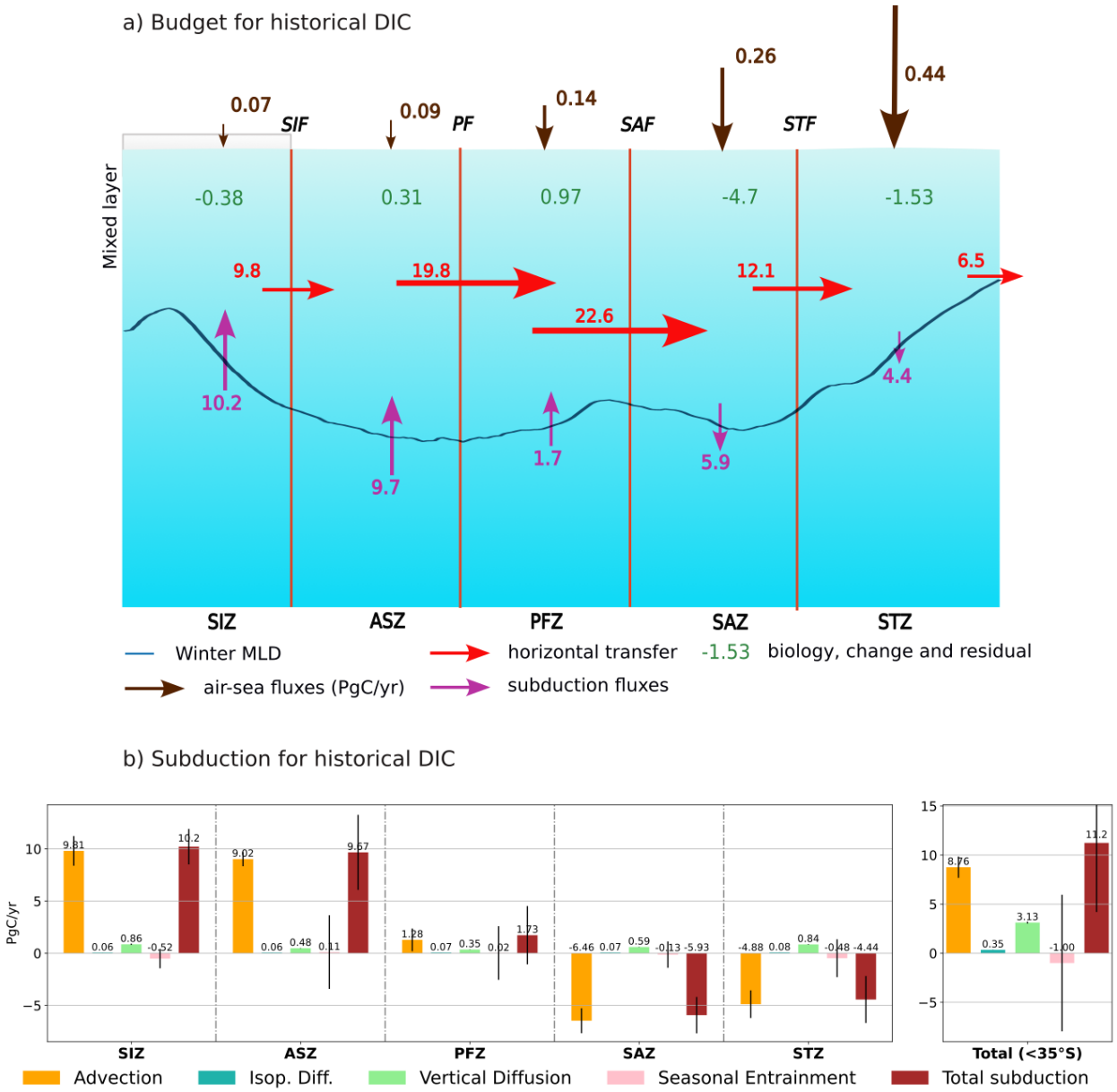

Figure 3.1: a) Budgets of historical DIC in the mixed layer averaged over 1995-2014 for each zone of the SO. The budget terms are computed following Eq. 2.3 and expressed in PgC/year. The size of arrows used for horizontal and mixed layer fluxes is 1/40 compared to the scale used for air-sea fluxes. The residual term is negative if DIC is consumed in the mixed layer (or because of uncertainties). b) Decomposition of subduction fluxes across the base of the mixed layer for each region into various processes following Eq. 2.2. Positive (negative) fluxes correspond to obduction (subduction). Zones in the SO are presented in Section 2.2.1.

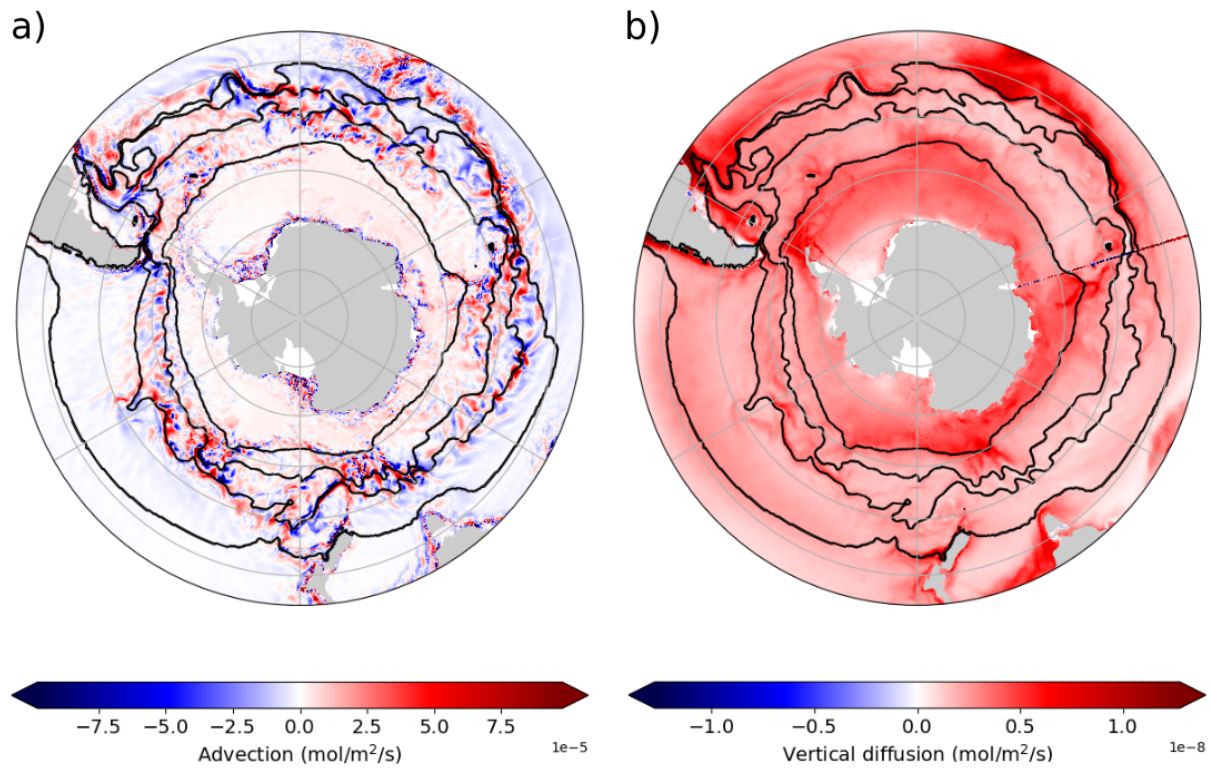

Figure 3.2: Maps of a) total advection and b) vertical diffusion fluxes of DIC_{hist} across the mixed layer base averaged over 1995-2014. Positive fluxes correspond to obduction. Contours correspond to the zones' boundaries.

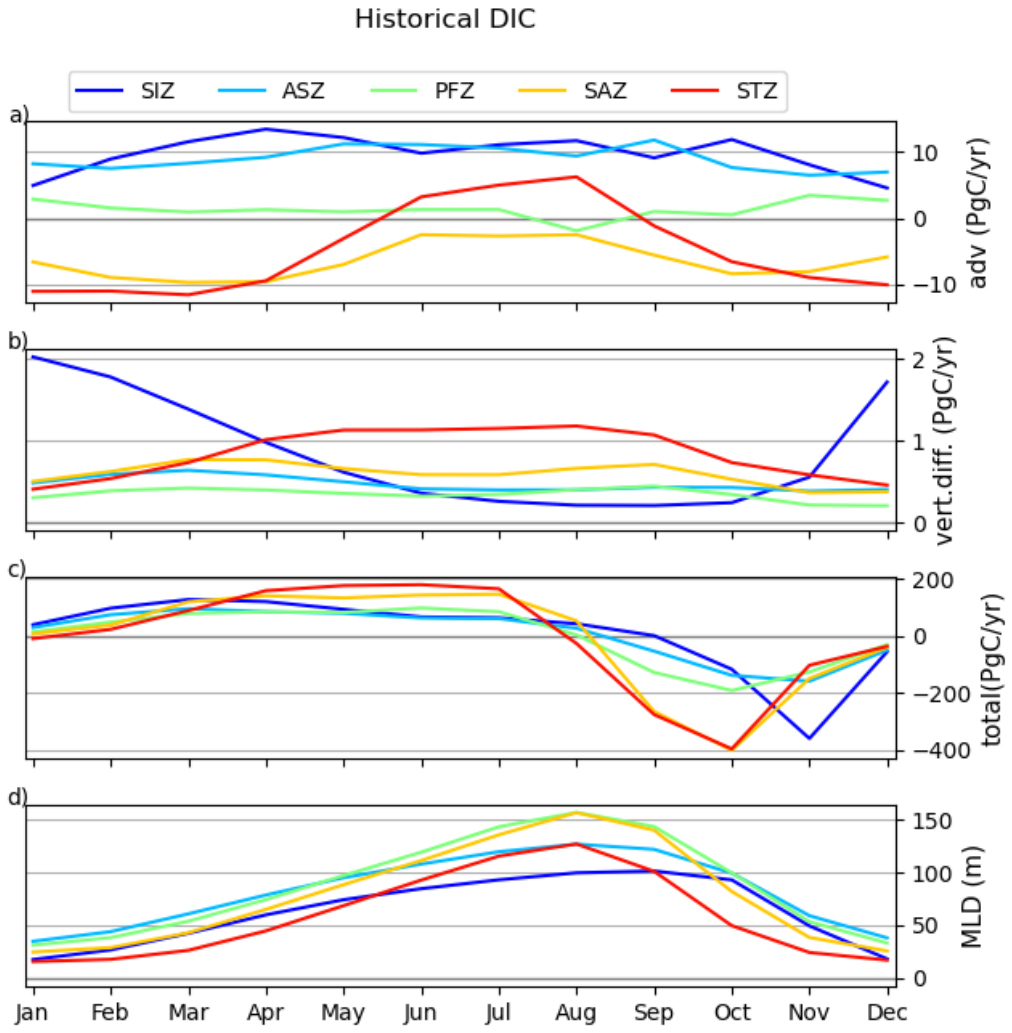

Figure 3.3: a-c) Seasonal climatology of the dominant processes driving the subduction of historical DIC across the mixed layer base. Positive values correspond to obduction. d) Seasonal climatology of the mixed layer depth with a criterion of 0.01 kg/m^3. Climatologies are computed over the 1995-2014 period for each zone of the SO.

by upwelling of Pacific, Indian and North Atlantic Deep Waters, it is not transferred to the atmosphere and is instead transported northward and then largely subducted north of the ACC.

Over the last 20 years of the simulation, neither the fluxes across region boundaries nor the DIC tendency show major interannual variability over the SO. This result agrees with Carroll et al. (2022), who found that their DIC tendency term is smaller in the SO than in other regions. In contrast, very large interannual variations in the DIC_{hist} subduction fluxes are found (Fig.S2.a) yet no significative trend appears over that period (Fig.S2.b).

The subduction fluxes are dominated by advection which represents the major part (85%) of obductive fluxes south of the SAF, and also the major part (84%) of the subductive fluxes north of the SAF (Fig 3.1.b). Therefore, advection drives the physical fluxes of historical DIC across the base of the mixed layer in all regions, but due to compensation between obductive in the south and subductive fluxes in the north, it only represents 67% of the total positive and negative fluxes averaged over the SO south of 35°S (Fig.3.1.b and Fig.3.2). Advective fluxes are homogeneously obducting DIC_{hist} in the SIZ and the ASZ, and subducting in the SAZ and the STZ (Fig.3.2.a). Hotspots of strong positive and negative advective fluxes appear within the PFZ and the SAZ, as well as the strong boundary currents such as the Agulhas Current (Fig.S10), which are known to be regions of high tracer subduction, linked with their high eddy kinetic energy (Sallée et al., 2012; Dove et al., 2021; Brady et al., 2021). In the STZ, stronger advective fluxes are also located in the Atlantic and the Indian Oceans (similarly to air-sea fluxes). As DIC_{hist} concentration increases with depth, vertical diffusion brings carbon within the mixed layer, representing 23% of the total physical transfer in the SO, which is a third of the contribution of advection on the whole region. Vertical diffusive fluxes are maximum at the SIF, where the melting of sea ice lead to strong stratification, and in western boundary currents (Fig.3.2.b). The remaining fluxes, seasonal entrainment and isopycnal diffusion, account for only 10% of total subduction in the SO. Isopycnal diffusion is mostly driven by vertical isopycnal diffusion (not shown), and hence mostly depends on the vertical gradient of DIC across the base of the mixed layer, similarly to vertical diffusion.

Drivers of the subduction vary at the seasonal scale (Fig.3.3). In the model, the summer minimum of MLD occurs in all regions in January, while the winter maximum occurs from August in the STZ to September in the SIZ. The seasonal variability is almost entirely dominated by the seasonal entrainment (see the total flux variability in Fig.3.3.d), with a peak of subduction at the beginning of spring (shoaling of the mixed layer) and a strong obduction in fall - winter (deepening of the mixed layer). Advective obduction also happens in winter

in the STZ, while subduction occurs the rest of the year. In the SIZ and the ASZ, carbon is obducted by advection throughout the year, obduction being greater in winter. Diffusive fluxes show strong/weak obduction in winter/summer in all regions except the SIZ, where the seasonality is reversed.

In conclusion, the physical driver of DIC_{hist} obduction is primarily advection, with a small contribution from vertical diffusion. DIC_{hist} is mainly obducted south of the SAF, then transported northward, where it is subducted north of the SAF and brought to lower latitudes to a lesser extent, following the circulation of water masses.

3.2 Anthropogenic Dissolved Inorganic Carbon

Anthropogenic DIC (DIC_{anth}) uptake at the surface ranges from 0.13 PgC/year to 0.18 PgC/year across the various regions (Fig.3.4.a). This narrow range results from the combination of the intensity of the fluxes and the size of the region, with the ASZ showing the largest fluxes while being one of the smallest regions. DIC_{anth} uptaken at the surface of the SO represents 81% of the DIC $_{anth}$ subducted below the mixed layer, the remaining 19% being brought from the subtropical regions north of 35°S. More specifically, our analyses show that a northward transport driven by Ekman transport brings DIC_{anth} across our zones' boundaries from the SIZ to the PFZ, while a southward transport brings DIC_{anth} to the STZ from outside the SO, where relatively warm and anthropogenic carbon-rich warm subtropical waters are found (Fig.2.8). These fluxes lead to small accumulations of DIC_{anth} in the SAZ and the STZ's mixed layer, where most of the subduction occurs, while keeping the southernmost regions depleted. The largest uncertainties hold in the horizontal fluxes, as they are computed as the residual of the other budget terms.
Over 1995-2004, the mixed layer DIC_{anth} content shows a weak interannual variability but does not show any trend (negligible tendency, as seen in Fig.3.4.a). However, DIC_{anth} air-sea fluxes show some significant trend (with the r-squared $r^2>0.9$), which is positive as expected since we increase the atmospheric pCO_2 (Fig.S3.b). A trend also appears in the subduction fluxes, with almost the same magnitude or even amplified (0.02 PgC/year^{-2} compared to 0.015 PgC/year^{-2} for the air-sea fluxes), but is not significant ($r^2<0.5$) given the high interannual variability of the subduction fluxes.

The subduction of DIC_{anth} within the SO amounts to 1.05PgC/year (Fig.3.4.b). 71% of the total subduction of DIC_{ant} over the SO occurs in the SAZ and the STZ, explaining the deep penetration of the anthropogenic signal seen in these regions (Fig.2.8). In contrast, the

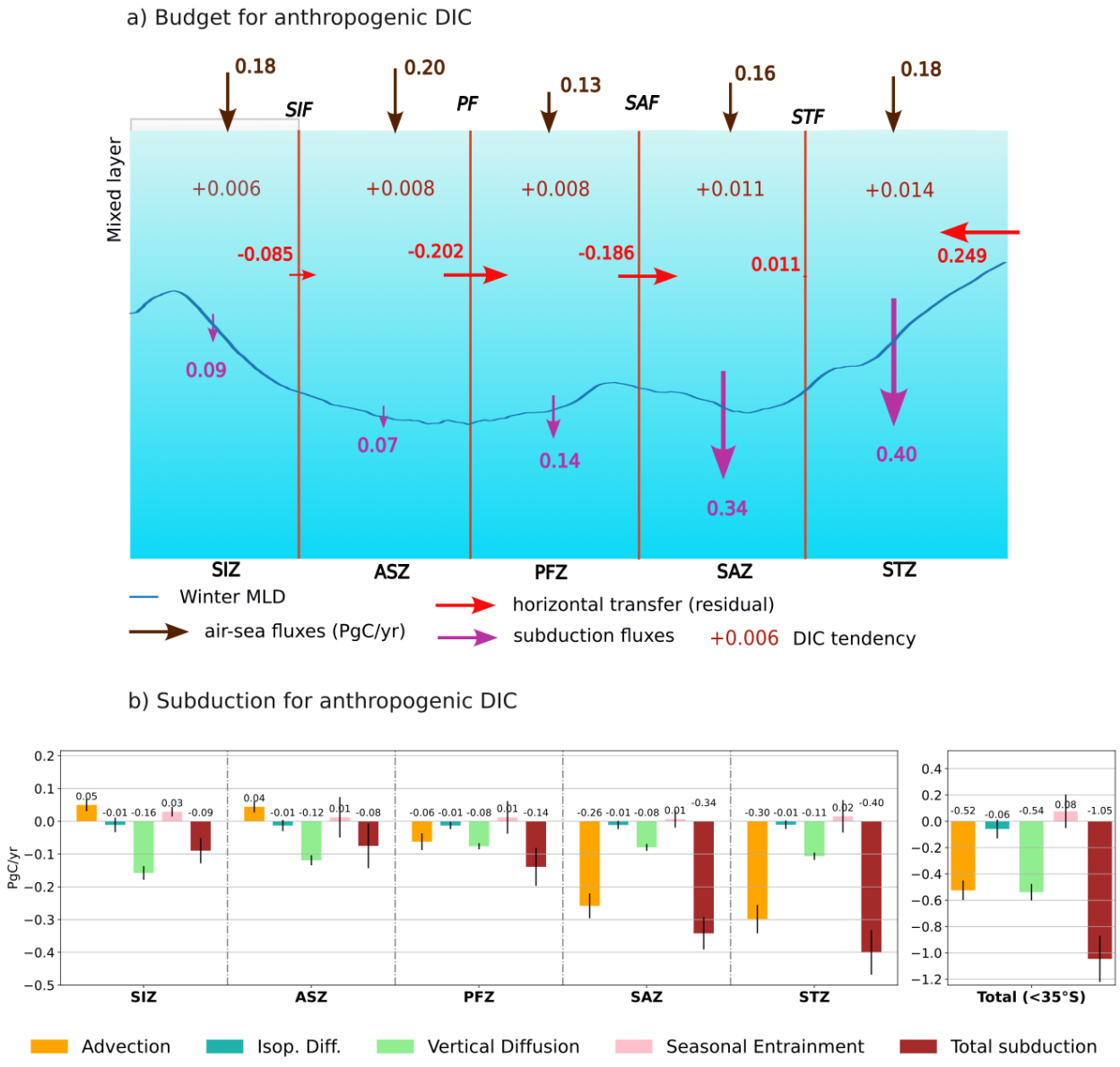

Figure 3.4: Same as Figure 3.1 but for DIC_{ant}. Here, air-sea fluxes use the same scale as the other fluxes. Horizontal fluxes are computed as the residual of our budgets.

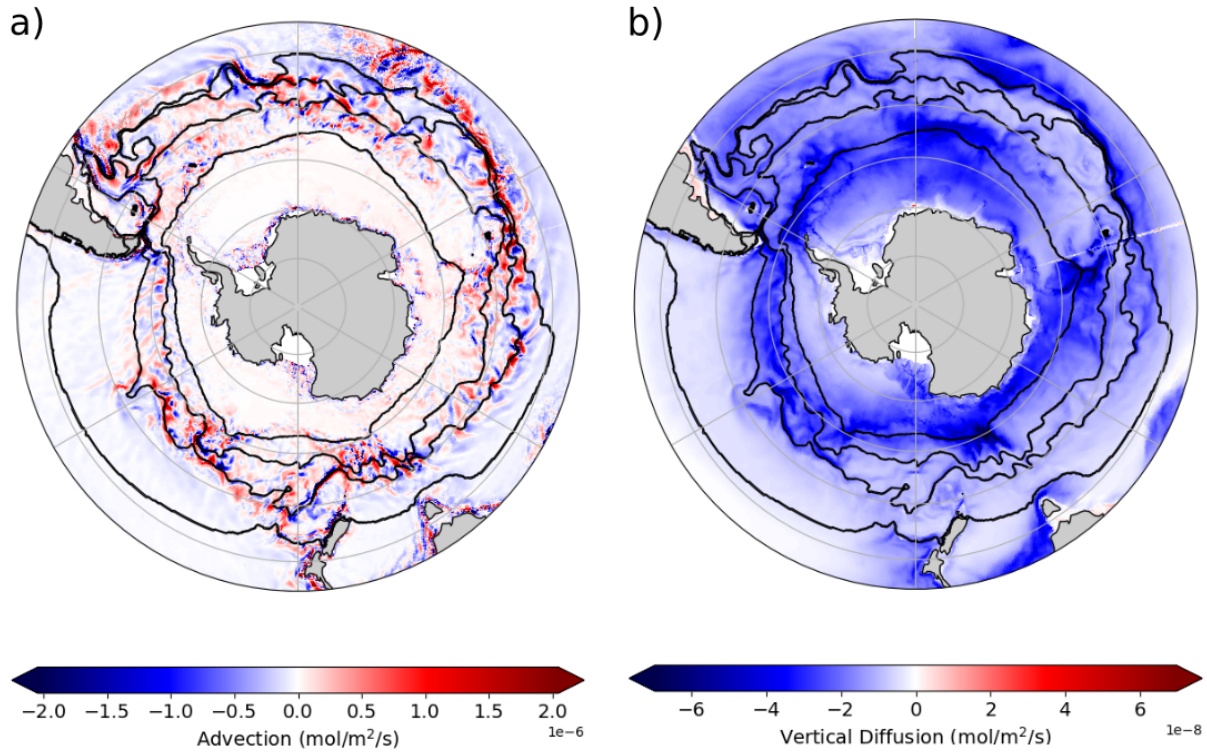

Figure 3.5: same as Fig. 3.2 for DIC_{ant}.

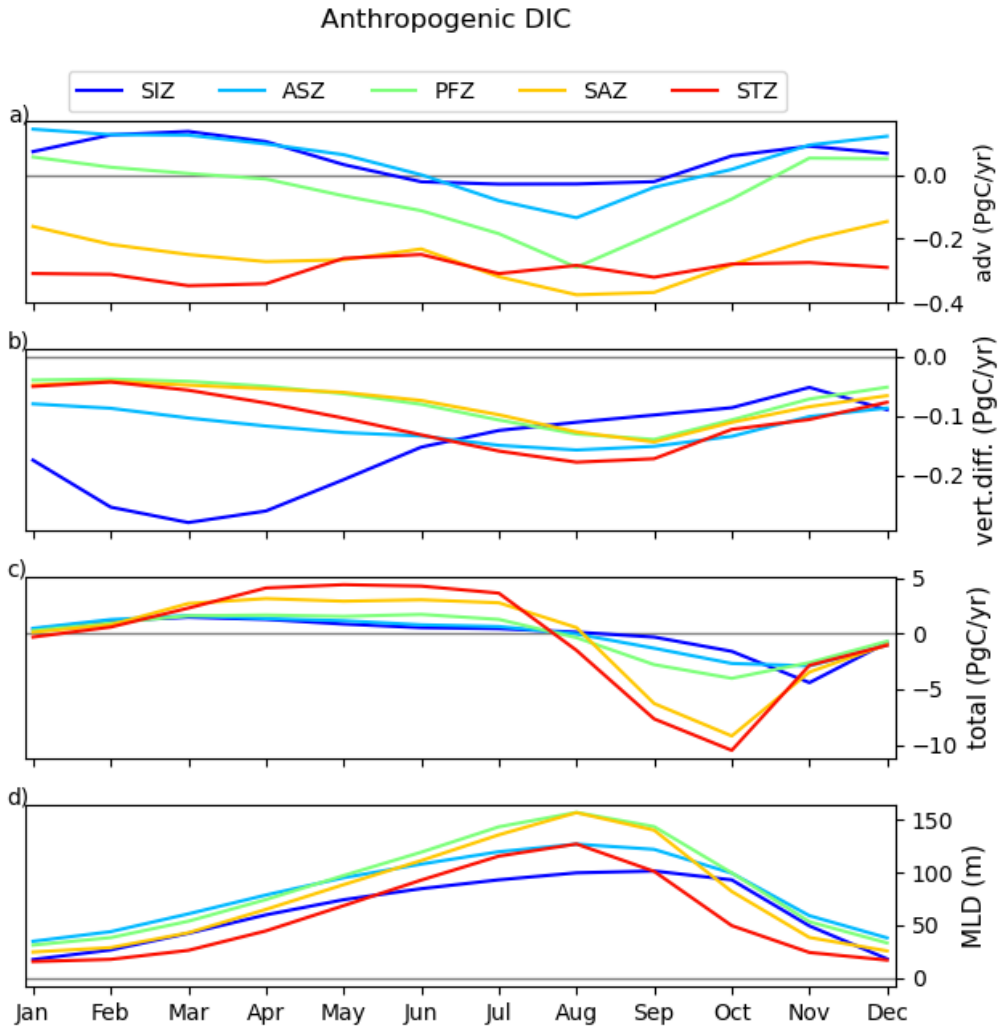

Figure 3.6: Seasonal climatology over the period 1995-2014 of the major subdubction fluxes. See Fig.3.3.

SIZ, ASZ, and to a lesser extent the PFZ, show the smallest subduction rates. When averaged over the SO, subduction is mainly achieved through vertical diffusion and advection, which each contribute to about half of the total flux of anthropogenic carbon towards the ocean interior. While advective fluxes dominate north of the ACC accounting for 69% of the total fluxes (over the sum of the absolute value of each flux) in the SAZ and STZ, vertical diffusion dominates south of the ACC, accounting for 62% of all the fluxes summed in absolute values in the SIZ, the ASZ and the PFZ. As expected, advection brings anthropogenic carbon within the mixed layer in the southernmost regions (SIZ, ASZ) due to the large-scale upwelling, and transfers carbon into the ocean interior in the northernmost regions (SAZ, STZ) through downwelling. In contrast, vertical diffusion acts to transfer anthropogenic carbon below the mixed layer in all regions, due to the upward vertical gradient of DIC_{anth}. Advective fluxes of DIC_{anth} follow the pattern of DIC_{hist}, with strong localized fluxes in the PFZ, SAZ and the boundary currents, as they depend on the circulation and mixed layer slope, and vertical diffusive fluxes are more closely linked to fronts and high eddy kinetic energy regions (Fig.3.5). The predominance of vertical diffusion in southern regions arises from the strong gradient of anthropogenic DIC across the mixed layer base (from 0 m to 500 m, with no deep convection on a monthly average scale). Seasonal entrainment is opposed to the gradient of anthropogenic DIC and brings the latter back into the mixed layer on a yearly average (net contribution), accounting for 7% of the sum of all fluxes. This result is not statistically significant due to the large interannual variability of this flux (some years, seasonal entrainment drives a net DIC_{anth} amount out of the mixed layer). Isopycnal diffusion follows the vertical gradient of anthropogenic DIC and is almost negligible, representing only 5% of the total.

The seasonality of DIC_{anth} fluxes across the mixed layer base is also driven by the seasonal entrainment with subduction/obduction following the shoaling/deepening of the ML (Fig.3.6.c). The seasonality of advective fluxes of DIC_{anth} is in the opposite phase compared to that of DIC_{hist} (with obduction in summer and subduction in winter), as the vertical gradient is opposite (Fig.3.6.a). The seasonality of vertical diffusion of DIC_{anth} is strongest in the SIZ, with a very large subduction at the end of the summer (Fig.3.6.c). A possible explanation for this signal is the accumulation of DIC_{anth} in the mixed layer over the summer and therefore a maximum vertical gradient around March. The vertical diffusion coefficient must also be larger in summer in the SIZ when winds can impact the upper layer of the ocean. Other regions show larger subduction at the end of winter, following the largest seasonal uptake driven by high solubility, and energy input by the winds hence a higher diffusion coefficient.

In summary, once uptaken in every region, DIC_{anth} is mostly subducted in the SAZ and the STZ. The physical drivers of DIC_{anth} subduction are primarily vertical diffusion south of the PF, and advection north of the SAF.

3.3 Total Organic Carbon (TOC)

TOC is produced in all regions (Fig.3.7.a), but especially in high Net Primary Production (NPP) regions such as the SAZ and the STZ (Fig.S4). TOC produced in the SIZ, the ASZ and the PFZ is subducted in the ASZ and the PFZ (0.217 PgC/year) but also transported for about one-third into the SAZ (0.144 PgC/year). In the SAZ, TOC is subducted (0.307 PgC/year), sinks (0.521 PgC/year) and is partially transported into the STZ (0.101 PgC/year). The STZ is the region where the most subduction occurs through physical transfer (0.479 PgC/year) and sedimentation (0.718 PgC/year). TOC fluxes' interannual variability is almost non-existent (Fig. S7).

All regions but the SIZ show a subduction of TOC across the mixed layer. The obduction in the SIZ is mostly achieved through advection and seasonal entrainment that bring TOC to the surface. Of the processes driving TOC subduction across the mixed layer base, vertical diffusion and advection are the dominant ones (respectively, 0.52±0.01 PgC/year i.e. 44% and 0.50 PgC/year i.e. 42% of all the fluxes summed in absolute values), showing the same patterns as DIC (Fig.3.8.a and b). One exception is the stronger TOC vertical diffusion, less seen in the DIC flux, in western boundary currents. Most of the subduction of TOC occurs in the STZ and SAZ (82.8% of the total sum i.e. -0.78 PgC/year), which is significant as they represent 48.7% of the total ocean surface of the SO south of 35°S.
Our analyses reveal that sedimentation (the only process of the gravitational pump) is the dominant driver of organic carbon particles and plankton transfer through the base of the mixed layer (1.97 PgC/year over the SO, Fig. 3.7b), being twice as large as the transfer achieved through physical transfer. Sedimentation predominates in regions of high productivity such as western boundary currents (Argentinian eastern coast, Agulhas Current, East Australian Current, Brazil Current; Fig.3.8.d). While sedimentation supports most of the transfer to depth in the SIZ and the ASZ (the physical transfer being around 1/4 and 1/3 of the sedimentation respectively), the role of the physical transfer increases with latitude, reaching up to 67% of that of the sedimentation in the STZ, for an average rate of 0.95 PgC/year over the SO. Spatially, the physical transfer dominates over sedimentation in high EKE regions (Fig.3.8.c).

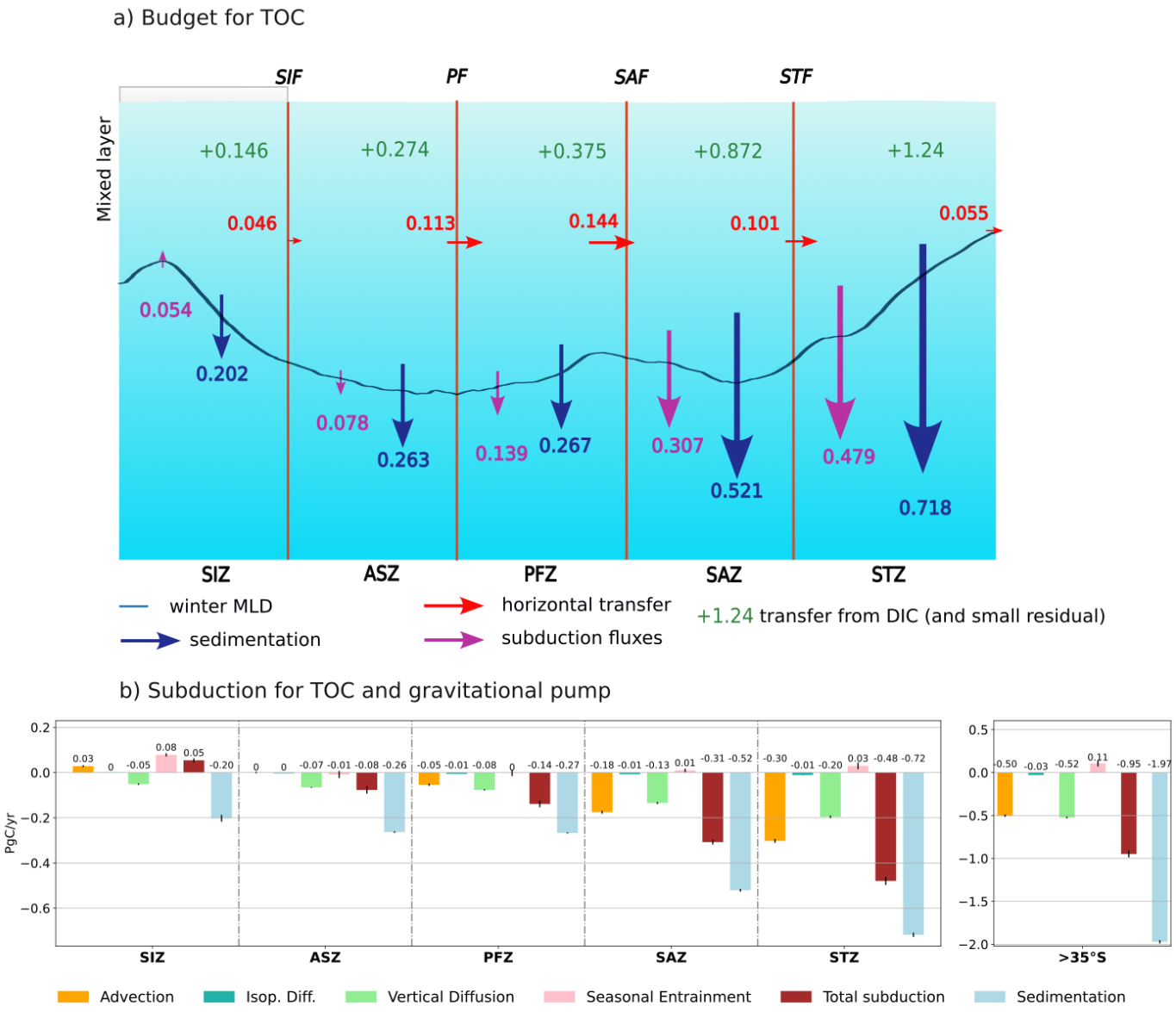

Figure 3.7: Same as Figure 3.1 but for TOC. The transfer of TOC through sedimentation is also indicated.

It is important to observe that while POC can sediment after subduction, DOC cannot (same behavior as for DIC), therefore it is interesting to also analyze them individually. Their roles in the subduction of organic carbon is pretty similar in total (0.51 PgC/year for DOC compared to 0.44 PgC/year for POC). DOC subduction dominates that of POC south of the STF, while POC subduction dominates in the STZ. The main difference between POC and DOC is observed for the seasonal entrainment: while this process subducts DOC, it obducts quite significantly POC in the STZ.

The transfer of TOC through sedimentation is maximum in spring (Fig.3.9), i.e. during the bloom season, with a peak occurring later in the season as we go southwards. In the SIZ, this transfer is maximum in January corresponding to the sea ice retreat. The PFZ and the ASZ show a muted seasonal cycle compared to the other regions. The seasonality of the TOC subduction follows that of the entrainment at the base of the mixed layer, similar to the DIC. Advective fluxes show a maximum in the middle of winter and higher seasonal amplitude as latitude decreases, while vertical diffusion shows a maximum when the mixed layer is deepest or starts shoaling, except in the SIZ where the maximum occurs during the deepening.

In summary, TOC is produced in most regions and primarily transferred below the mixed layer base afterward. Production and transfer decrease with latitude. Physical transfer accounts for around half of the sedimentation with a predominance of the latter mostly south of the SAF.

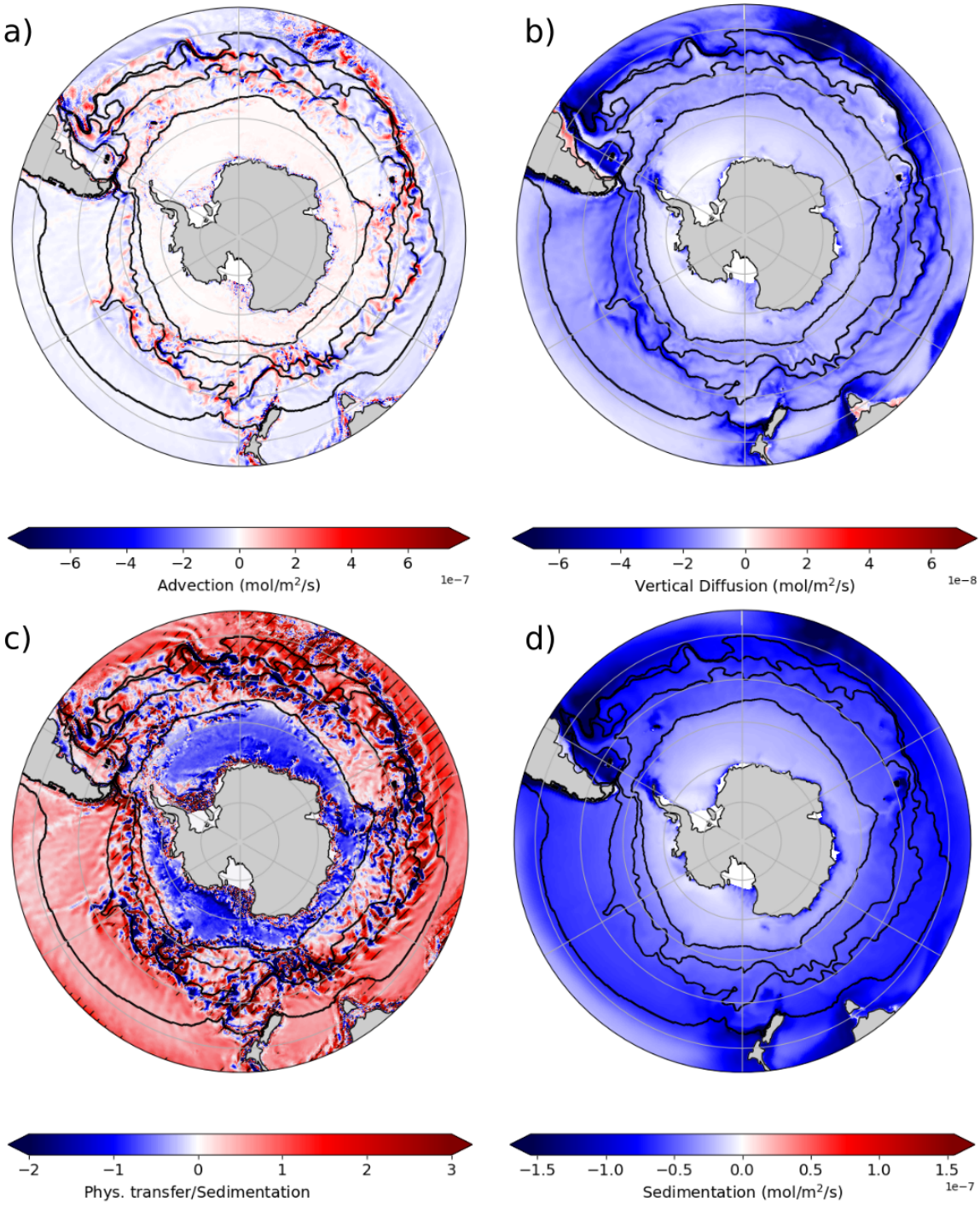

Figure 3.8: Maps of a) advection, b) vertical diffusion fluxes, c) physical transfer over sedimentation and d) sedimentation for TOC averaged over 1995-2014. Positive fluxes correspond to obduction in a, b and d. In c), positive numbers correspond to similar sign for physical transfer and sedimentation, and black hatches indicate regions where subduction is higher than sedimentation.

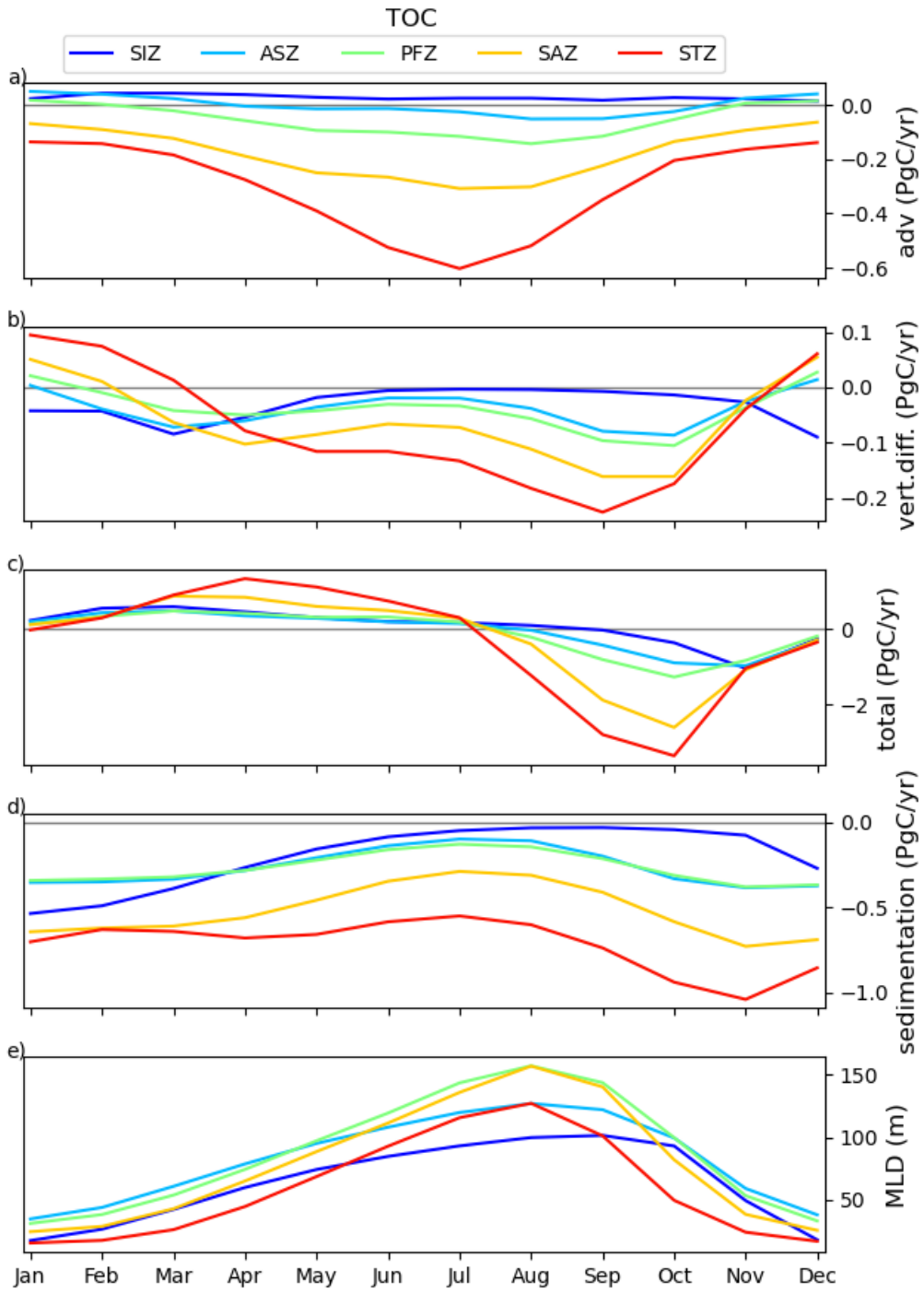

Figure 3.9: Seasonal climatology over the period 1995-2014 of the major subduction fluxes and the sedimentation, with the same sign convention as Fig.3.3.

Chapter 4

Discussion

Using a new configuration of the NEMO-PISCES model at 0.25° resolution, we have analyzed the DIC_{hist}, DIC_{anth} and TOC fluxes in the mixed layer, and detailed in particular the fluxes at the base of the mixed layer. These analyses differ from previous studies using lower resolution models (Toyama et al., 2017; Bopp et al., 2015; Levy et al., 2013; Iudicone et al., 2011) and observations (Sauvé et al., 2023), in terms of the magnitude of the carbon subduction rates and of which processes dominate the transfer through the mixed layer base.

Most modeling studies so far have investigated the subduction of preindustrial or anthropogenic DIC. We note that preindustrial DIC fluxes are very close to historical DIC fluxes at the mixed layer base, given the relatively small contribution of anthropogenic carbon fluxes to historical fluxes.

South of 44°S, Levy et al. (2013) obtain a preindustrial DIC obduction of 14.3 PgC/year, while we obtain a much higher obduction of 22.8 PgC/year. Levy et al. (2013) used a 2° global NEMO-PISCES model with the same online subduction diagnostics as the present study. This larger obduction is due to a larger advection term in our study (corresponding to their advection and eddy mixing terms - GM) of ∼20 PgC/year compared to ∼12 PgC/year. Our vertical mixing term of ∼2 PgC/year is similar to what they obtain. The difference between advection terms might be explained by a more energetic circulation due to the higher resolution of our model leading to more intense advective fluxes at the base of the mixed layer. Kamenkovich et al. (2017) have also shown that eddies largely impact the SO ventilation (with off-line tracers). Our advection and vertical mixing terms also differ from Iudicone et al. (2011), for each zone. Using a lagrangian framework, they find similar advection (Ekman transport in their case) in most of the zones but the SIZ, but much smaller vertical mixing rates (on the order of 5 to 10 PgC/year versus 1 PgC/year). This large difference might also come from the difference in the surface on which the fluxes are computed (the mixed layer in the SAZ for us and the water masses density levels for them). As for

fluxes within the mixed layer, Iudicone et al. (2011) show that preindustrial DIC is imported from subtropical regions at 30°S and at the STF within the SO mixed layer (their Fig.3 and Fig.6). This result contrasts with what we find which is a consistent northward transport of DIC across all fronts of the ACC bringing a fraction of the DIC, initially brought to the surface layer within the SO, north of 35°S within the mixed layer. Whether this discrepancy arises from the Lagrangian method used in Iudicone et al. (2011) or from the aspects internal to the model is unclear.

Our analyses show that vertical diffusion and advection contribute equally to the subduction of DIC_{anth} below the mixed layer. However, if we integrate the contributions south of 44°S, vertical diffusion is found to dominate largely over other physical processes (0.42 PgC/year for vertical diffusion compared to around 0.05 PgC/year for advection and isopycnal diffusion, and -0.06 PgC/year for seasonal entrainment). This result corroborates that from Bopp et al. (2015) who found that vertical mixing (resulting from vertical diffusion, seasonal entrainment and isopycnal diffusion) is the main driver of subduction. In their 2° resolution NEMO-PISCES model, using the same online diagnostics, the subduction rate by vertical mixing is 0.69 PgC/year, a value somewhat larger than our rate of 0.40 PgC/year.

In contrast with the similarity found for the vertical diffusion term, the advection term (that they decompose unlike us in resolved + parametrized mesocale with the GM parametrization) is much stronger in the model of Bopp et al. (2015) than ours (-0.3 PgC/year versus 0.055 PgC/year). The sign is also different, which could be explained by small differences in the circulation, as we are looking at small net residuals after averaging much larger local advective fluxes. Note that the role of advection is low south of 44°S because obduction in the SIZ and the ASZ compensate for subduction in the PFZ and part of the SAZ. In our model, the SAZ and STZ host the largest subduction fluxes of anthropogenic DIC supported by advection. This region sees the cooling and transformation of Subtropical Waters (STW), rich in DIC_{anth} into SAMW, which are subducted as part of the upper cell on the Southern Ocean overturning circulation. It is where Groeskamp et al. (2016), using a diathermohaline stream function framework, found that the majority of subduction of DIC_{anth} occurs through advection.

At the SAF, the transport of DIC_{anth} within the mixed layer is directed northward and amounts to ∼0.19 PgC/year, which appears in line with the study of DeVries (2014) (based on an ocean circulation inverse model at 2°) who found a northward flux of 0.30 PgC/year at 44°S (which is the approximate latitude of the STF but the SAF is close, at 49°S) over the whole column. At the northern boundary of the SO, the anthropogenic DIC transport is directed southward in our model while it remains northward in theirs. This difference

might arise from the northward transport of anthropogenic DIC within the SAMW below the mixed layer that we do not account for in our analyses.

Our DIC_{hist} fluxes across the mixed layer base can be compared to estimates made from BGC-Argo float measurements by Sauvé et al. (2023). While Sauvé et al. (2023) find a much stronger vertical diffusion in the ASZ than in the SIZ (2.4 compared to 0.64 mol/m^2/year), we find a vertical diffusion in the ASZ similar to them (2.7 mol/m^2/year) but a much stronger diffusion in the SIZ (3.5 mol/m^2/year). These differences could point to a misrepresentation of DIC_{hist} gradients (which are very strong due to melting of sea ice - not shown) or of the mixing (different diffusion coefficients) in the SIZ in our model. Our advective fluxes in the SIZ and the ASZ are also smaller than in Sauvé et al. (2023): while they find an advection of around 80 mol/m^2/year in both regions, our fluxes reach 40.3 mol/m^2/year in the SIZ and 50.3 mol/m^2/year in the ASZ, thus a difference of around 40%. Yet, our advective fluxes are much stronger than that of previous studies base on coarse-resolution models (e.g. Levy et al., 2013) hence suggesting that increasing the resolution draw us closer to observations.

Discrepancies with estimates from BGC-Argo floats are especially large for the fluxes are the air-sea interface, and could explain partially the discrepancies with Sauvé et al. (2023) budget for mixed layer fluxes. Our model, such as numerous ocean models (Mongwe et al., 2018; Hauck et al., 2020), shows an uptake in all regions all year long except a short period in summer and fall, while Gray et al. (2018) find outgassing in the southernmost regions, especially in winter. However, our model aligns better with fluxes derived from ship-based measurements, which find a large uptake in the recent years (Bushinsky et al., 2019). The new Argo floats dataset has a different sampling than ship-based climatologies, with more measurements in southernmost regions in winter, yet, biases could remain as well as errors in the reconstructions. For that reason, Bushinsky et al. (2019) combine all observational datasets, finding on average a reduced uptake compared to ship-based measurements only. They indicate that the difference between these datasets is not yet determined to be an over/underestimation of the outgassing of natural carbon or the uptake of anthropogenic carbon.

The need for taking into account the subduction of DOC and POC below the mixed layer to obtain a more robust estimate of carbon export has been underlined in several studies recently (Stukel and Ducklow, 2017; Boyd et al., 2019; Giering et al., 2023). Here, we have quantified the different mechanisms of organic carbon export across five zones of the SO.

We found that south of 44°S, TOC (POC+DOC) is mainly subducted through vertical diffusion (0.15 PgC/year) and advection (0.13 PgC/year) while it is slightly obducted by seasonal entrainment (-0.07 PgC/year). Combining vertical diffusion and seasonal entrain-

ment gives a vertical mixing of 0.08 PgC/year. The relative contributions of vertical mixing and advection to the transfer of organic carbon to the ocean interior we have calculated are opposite to that found in Levy et al. (2013). For them, vertical mixing dominates largely at a rate of ∼0.7 PgC/year, while advection (again corresponding to their advection and eddy mixing terms) represents an obduction of only ∼0.05 PgC/year. In the temperate Southern Hemisphere (between 18°S and 44°S), the role of advection is again far more predominant in our simulations compared to vertical mixing, while vertical mixing and advection have similar roles in Levy et al. (2013). The transfer of organic carbon by sedimentation is, however, similar between the two studies (1.12 PgC/year in our study and 1.4 PgC/year in Levy et al. (2013)). We, therefore, conclude that the main differences between our studies are a much smaller total subduction in our case (around one-third of theirs), driven by both advection and vertical diffusion, and a smaller relative role of the TOC subduction (physical transfer) compared to the sedimentation (biological transfer; 20% in our case and 42% in Levy et al. (2013)).

In the North Atlantic, Resplandy et al. (2019), using the NEMO-LOBSTER model show, as Levy et al. (2013), that subduction is dominated by the vertical diffusion (which they call mixed layer pump). In contrast to Levy et al. (2013), subduction represents around 25% of the gravitational pump in the subpolar region, a result that matches ours for the equivalent regions (SIZ, ASZ). Moreover, subduction reaches about half of the sedimentation in the jet, a result that we find for our PFZ and SAZ (equivalent regions for the Southern Hemisphere). There is however a difference with Resplandy et al. (2019) for the subtropics: whereas subduction represents again half of the sedimentation in their study, it is more important in ours (67%). We conclude that there are similarities between the Southern Ocean and the North Atlantic in terms of contribution to organic carbon export. Using a data assimilation model, Nowicki et al. (2022) found that the gravitational pump dominates in the SO, accounting for 75% of the total transfer of DOC to the interior, while the mixing pump, corresponding to our subduction, represents only 12%, the rest being attributed to the migrant pump. A partial explanation for this disagreement with our results is that their model does not represent the subduction of POC but only of DOC. In our model, DOC and POC have similar contributions, which show that the latter should not be neglected. This study underlines the fact that our model lacks the representation of the migrant pump to obtain a complete picture. Indeed, Stukel et al. (2023) also find a significant migrant pump in the Californian coastal upwelling using observations. Moreover, they show that organic carbon export by the gravitational pump allows more carbon sequestration at depth than the subduction, representing 42% of the sequestration between 100 m and 400 m, but only 13% between 400 m and 1000 m, and almost none below 1000 m.

While our study shows a higher physical transfer and sedimentation in the SAZ and the STZ, it can resurface within a few years in such subtropical areas. On the other end, sequestration times are higher at high latitudes, where the sedimentation dominates, with the formation of AABW (Boyd et al., 2019; Nowicki et al., 2022). Therefore, on longer timescales, the SO physical pump might be less important, and the sedimentation, stronger in higher latitudes in our model, would dominate even more.

Relative roles of the subduction and gravitational pump vary regionally (Fig.3.8.c): subduction predominates over the sedimentation in frontal regions (ASZ, PFZ) and regions of high productivity (western boundary currents, coastal area). This result corroborates studies from (Stukel and Ducklow, 2017), showing a stronger role of vertical mixing in highly productive regions for organic matter (from one-quarter to one-half). It also aligns with the spatial variability in the subduction of all tracers (DIC, DOC, POC), with higher subduction in frontal/high EKE regions (Freilich and Mahadevan, 2021; Balwada et al., 2018).

Summer carbon export by the biological pump is predicted to increase over the 21st century due to increased iron input by dust deposition and warming (Bazzani et al., 2023), which would likely strengthen the TOC uptake (Henson et al., 2022). However, our study shows that north of the PF, the biological pump is also driven by advection and vertical diffusion of TOC and POC. Changes in circulation and stratification may thus oppose that in sedimentation with a net effect that is yet to be determined.

Chapter 5

Conclusion

In this study, I have used an eddying global ocean model to calculate subduction fluxes of inorganic and organic carbon across the base of the mixed layer. The model configuration has a resolution of 0.25° which allows the partial resolution of mesoscale eddies in the Southern Ocean. The simulations make use of an online diagnostic tool to calculate the contribution of each process to the subduction of DIC and TOC (DOC+POC) across the mixed layer base at each time step of the model, along with the sinking rate (sedimentation) of POC. Two simulations with the same circulation but different CO_2 atmospheric concentrations were used to contrast the historical and anthropogenic DIC fluxes. The main results are the following:

1. Advection was found to be the main process driving DIC_{hist} across the mixed layer. South of the SAF, advection drives DIC_{hist} obduction into the mixed layer, where it is transported northward through the SAF. North of the SAF, advection drives the subduction, partly countered by obduction by vertical diffusion. Part of the historical DIC in the STZ is transported to lower latitudes within the mixed layer.

2. Once taken up at the surface of the SO, anthropogenic DIC is mostly subducted through vertical diffusion south of the PF, with a small obduction by advection. In the PFZ, advection and vertical diffusion both act to subduct anthropogenic DIC, while north of the SAF, advection is the main driver of subduction. This leads to equal roles of vertical diffusion and advection in the subduction of anthropogenic carbon in the SO.

3. Sedimentation represents two-thirds of the transfer of organic carbon below the mixed layer with subduction being responsible for the remainder. Organic carbon is transferred mostly by sedimentation south of the SAF, while the subduction accounts for around 60% of the sedimentation north of the SAF, where TOC concentration is more

important. Over the SO, the subduction of organic carbon is equally driven by advection and vertical diffusion.

4. In total, 11.2 PgC/year of historical DIC is obducted into the mixed layer, while 2.9 PgC/year of TOC is subducted below. Combining both gives a carbon flux into the mixed layer of 8.3 PgC/year south of 35°S. This number does not show a trend during the 10 years investigated.

5. Our model-based analyses confirm recent observation-based results obtained as part of the SOLACE campaign (https://solace2020.net/) suggesting that the subduction (physical transfer) of organic carbon to the interior plays a role potentially almost as important as that of the sedimentation (see Appendix 2). More measurements are required to perform an accurate quantification of the respective roles of the physical versus the biological transfer of organic carbon in the subduction rates.

Chapter 6

Bibliography

Adcroft, A., Anderson, W., Balaji, V., Blanton, C., Bushuk, M., Dufour, C. O., Dunne, J. P., Griffies, S. M., Hallberg, R., Harrison, M. J., Held, I. M., Jansen, M. F., John, J. G., Krasting, J. P., Langenhorst, A. R., Legg, S., Liang, Z., McHugh, C., Radhakrishnan, A., Reichl, B. G., Rosati, T., Samuels, B. L., Shao, A., Stouffer, R., Winton, M., Wittenberg, A. T., Xiang, B., Zadeh, N., and Zhang, R. (2019). The GFDL Global Ocean and Sea Ice Model OM4.0: Model Description and Simulation Features. *Journal of Advances in Modeling Earth Systems*, 11(10):3167–3211.

Aumont, O., Ethé, C., Tagliabue, A., Bopp, L., and Gehlen, M. (2015). PISCES-v2: an ocean biogeochemical model for carbon and ecosystem studies. *Geoscientific Model Development*, 8(8):2465–2513.

Balwada, D., Smith, K. S., and Abernathey, R. (2018). Submesoscale Vertical Velocities Enhance Tracer Subduction in an Idealized Antarctic Circumpolar Current. *Geophysical Research Letters*, 45(18):9790–9802.

Bazzani, E., Lauritano, C., and Saggiomo, M. (2023). Southern Ocean Iron Limitation of Primary Production between Past Knowledge and Future Projections. *Journal of Marine Science and Engineering*, 11(2):272.

Blanke, B. and Delecluse, P. (1993). Variability of the Tropical Atlantic Ocean Simulated by a General Circulation Model with Two Different Mixed-Layer Physics. *Journal of Physical Oceanography*, 23:1363–1388.

Bopp, L., Lévy, M., Resplandy, L., and Sallée, J. B. (2015). Pathways of anthropogenic carbon subduction in the global ocean. *Geophysical Research Letters*, 42(15):6416–6423.

Boyd, P. W., Claustre, H., Levy, M., Siegel, D. A., and Weber, T. (2019). Multi-faceted particle pumps drive carbon sequestration in the ocean. *Nature*, 568(7752):327–335.

Brady, R. X., Maltrud, M. E., Wolfram, P. J., Drake, H. F., and Lovenduski, N. S. (2021). The Influence of Ocean Topography on the Upwelling of Carbon in the Southern Ocean. *Geophysical Research Letters*, 48(19).

Bushinsky, S. M., Landschützer, P., Rödenbeck, C., Gray, A. R., Baker, D., Mazloff, M. R., Resplandy, L., Johnson, K. S., and Sarmiento, J. L. (2019). Reassessing Southern Ocean Air-Sea CO_2 Flux Estimates With the Addition of Biogeochemical Float Observations. *Global Biogeochemical Cycles*, 33(11):1370–1388.

Carroll, D., Menemenlis, D., Dutkiewicz, S., Lauderdale, J. M., Adkins, J. F., Bowman, K. W., Brix, H., Fenty, I., Gierach, M. M., Hill, C., Jahn, O., Landschützer, P., Manizza, M., Mazloff, M. R., Miller, C. E., Schimel, D. S., Verdy, A., Whitt, D. B., and Zhang, H. (2022). Attribution of Space-Time Variability in Global-Ocean Dissolved Inorganic Carbon. *Global Biogeochemical Cycles*, 36(3).

Chen, H., Morrison, A. K., Dufour, C. O., and Sarmiento, J. L. (2019). Deciphering Patterns and Drivers of Heat and Carbon Storage in the Southern Ocean. *Geophysical Research Letters*, 46(6):3359–3367.

de Boyer Montégut, C. (2004). Mixed layer depth over the global ocean: An examination of profile data and a profile-based climatology. *Journal of Geophysical Research*, 109(C12):C12003.

DeVries, T. (2014). The oceanic anthropogenic CO $_2$ sink: Storage, air-sea fluxes, and transports over the industrial era. *Global Biogeochemical Cycles*, 28(7):631–647.

DeVries, T., Holzer, M., and Primeau, F. (2017). Recent increase in oceanic carbon uptake driven by weaker upper-ocean overturning. *Nature*, 542(7640):215–218.

Dove, L. A., Thompson, A. F., Balwada, D., and Gray, A. R. (2021). Observational Evidence of Ventilation Hotspots in the Southern Ocean. *Journal of Geophysical Research: Oceans*, 126(7).

Drake, H. F., Morrison, A. K., Griffies, S. M., Sarmiento, J. L., Weijer, W., and Gray, A. R. (2018). Lagrangian Timescales of Southern Ocean Upwelling in a Hierarchy of Model Resolutions. *Geophysical Research Letters*, 45(2):891–898.

Dufour, C. O., Griffies, S. M., de Souza, G. F., Frenger, I., Morrison, A. K., Palter, J. B., Sarmiento, J. L., Galbraith, E. D., Dunne, J. P., Anderson, W. G., and Slater, R. D. (2015). Role of Mesoscale Eddies in Cross-Frontal Transport of Heat and Biogeochemical Tracers in the Southern Ocean. *Journal of Physical Oceanography*, 45(12):3057–3081.

Dufour, C. O., Le Sommer, J., Zika, J. D., Gehlen, M., Orr, J. C., Mathiot, P., and Barnier, B. (2012). Standing and Transient Eddies in the Response of the Southern Ocean Meridional Overturning to the Southern Annular Mode. *Journal of Climate*, 25(20):6958–6974.

Dufour, C. O., Sommer, J. L., Gehlen, M., Orr, J. C., Molines, J., Simeon, J., and Barnier, B. (2013). Eddy compensation and controls of the enhanced sea-to-air CO_2 flux during positive phases of the Southern Annular Mode. *Global Biogeochemical Cycles*, 27(3):950–961.

Dussin, R., Barnier, B., Brodeau, L., and Molines, J.-M. (2016). The Making Of the DRAKKAR FORCING SET DFS5.

Farneti, R., Delworth, T. L., Rosati, A. J., Griffies, S. M., and Zeng, F. (2010). The Role of Mesoscale Eddies in the Rectification of the Southern Ocean Response to Climate Change. *Journal of Physical Oceanography*, 40(7):1539–1557.

Freilich, M. and Mahadevan, A. (2021). Coherent Pathways for Subduction From the Surface Mixed Layer at Ocean Fronts. *Journal of Geophysical Research: Oceans*, 126(5).

Friedlingstein, P., O'Sullivan, M., and Jones, M. W. (2020). Global Carbon Budget 2020. *Earth System Science Data*, 12(4):3269–3340.

Frölicher, T. L., Sarmiento, J. L., Paynter, D. J., Dunne, J. P., Krasting, J. P., and Winton, M. (2015). Dominance of the Southern Ocean in Anthropogenic Carbon and Heat Uptake in CMIP5 Models. *Journal of Climate*, 28(2):862–886.

Gent, P. and McWilliams, J. (1990). Isopycnal Mixing in Ocean Circulation Models. *Journal of Physical Oceanography*, 20:150–155.

Gent, P., McWilliams, J., Willebrand, J., and McDougall, T. J. (1995). Parameterizing Eddy-Induced Tracer Transports in Ocean Circulation Models. *Journal of Physical Oceanography*, 25(4):463–474.

Giering, S., Sanders, R., Blackbird, S., Briggs, N., Carvalho, F., East, H., Espinola, B., Henson, S., Kiriakoulakis, K., Iversen, M., Lampitt, R., Pabortsava, K., Pebody, C., Peel, K., Preece, C., Saw, K., Villa-Alfageme, M., and Wolff, G. (2023). Vertical imbalance in

organic carbon budgets is indicative of a missing vertical transfer during a phytoplankton bloom near South Georgia (COMICS). *Deep Sea Research Part II: Topical Studies in Oceanography*, 209:105277.

Graven, H. D., Gruber, N., Key, R., Khatiwala, S., and Giraud, X. (2012). Changing controls on oceanic radiocarbon: New insights on shallow-to-deep ocean exchange and anthropogenic CO $_2$ uptake: CHANGING CONTROLS ON OCEANIC ^{14} C. *Journal of Geophysical Research: Oceans*, 117(C10):n/a–n/a.

Gray, A. R., Johnson, K. S., Bushinsky, S. M., Riser, S. C., Russell, J. L., Talley, L. D., Wanninkhof, R., Williams, N. L., and Sarmiento, J. L. (2018). Autonomous Biogeochemical Floats Detect Significant Carbon Dioxide Outgassing in the High-Latitude Southern Ocean. *Geophysical Research Letters*, 45(17):9049–9057.

Groeskamp, S., Lenton, A., Matear, R., Sloyan, B. M., and Langlais, C. (2016). Anthropogenic carbon in the ocean—Surface to interior connections. *Global Biogeochemical Cycles*, 30(11):1682–1698.

Gruber, N., Clement, D., Carter, B. R., Feely, R. A., Van Heuven, S., Hoppema, M., Ishii, M., Key, R. M., Kozyr, A., Lauvset, S. K., Lo Monaco, C., Mathis, J. T., Murata, A., Olsen, A., Perez, F. F., Sabine, C. L., Tanhua, T., and Wanninkhof, R. (2019a). The oceanic sink for anthropogenic CO $_2$ from 1994 to 2007. *Science*, 363(6432):1193–1199.

Gruber, N., Gloor, M., Mikaloff Fletcher, S. E., Doney, S. C., Dutkiewicz, S., Follows, M. J., Gerber, M., Jacobson, A. R., Joos, F., Lindsay, K., Menemenlis, D., Mouchet, A., Müller, S. A., Sarmiento, J. L., and Takahashi, T. (2009). Oceanic sources, sinks, and transport of atmospheric CO_2: OCEANIC SOURCES, SINKS AND TRANSPORT OF CO_2. *Global Biogeochemical Cycles*, 23(1):n/a–n/a.

Gruber, N., Landschützer, P., and Lovenduski, N. S. (2019b). The Variable Southern Ocean Carbon Sink. *Annual Review of Marine Science*, 11(1):159–186. _eprint: https://doi.org/10.1146/annurev-marine-121916-063407.

Hallberg, R. (2013). Using a resolution function to regulate parameterizations of oceanic mesoscale eddy effects. *Ocean Modelling*, 72:92–103.

Hallberg, R. and Gnanadesikan, A. (2006). The Role of Eddies in Determining the Structure and Response of the Wind-Driven Southern Hemisphere Overturning: Results from the Modeling Eddies in the Southern Ocean (MESO) Project. *Journal of Physical Oceanography*, 36(12):2232–2252.

Hauck, J., Zeising, M., Le Quéré, C., Gruber, N., Bakker, D. C. E., Bopp, L., Chau, T. T. T., Gürses, , Ilyina, T., Landschützer, P., Lenton, A., Resplandy, L., Rödenbeck, C., Schwinger, J., and Séférian, R. (2020). Consistency and Challenges in the Ocean Carbon Sink Estimate for the Global Carbon Budget. *Frontiers in Marine Science*, 7:571720.

Henson, S. A., Laufkötter, C., Leung, S., Giering, S. L. C., Palevsky, H. I., and Cavan, E. L. (2022). Uncertain response of ocean biological carbon export in a changing world. *Nature Geoscience*, 15(4):248–254.

Hosoda, S., Ohira, T., Sato, K., and Suga, T. (2010). Improved description of global mixed-layer depth using Argo profiling floats. *Journal of Oceanography*, 66(6):773–787.

Iudicone, D., Rodgers, K. B., Stendardo, I., Aumont, O., Madec, G., Bopp, L., Mangoni, O., and Ribera d'Alcala', M. (2011). Water masses as a unifying framework for understanding the Southern Ocean Carbon Cycle. *Biogeosciences*, 8(5):1031–1052.

Kamenkovich, I., Garraffo, Z., Pennel, R., and Fine, R. A. (2017). Importance of mesoscale eddies and mean circulation in ventilation of the Southern Ocean. *Journal of Geophysical Research: Oceans*, 122(4):2724–2741.

Karleskind, P., Lévy, M., and Memery, L. (2011). Subduction of carbon, nitrogen, and oxygen in the northeast Atlantic. *Journal of Geophysical Research*, 116(C2):C02025.

Lachkar, Z., Orr, J. C., Dutay, J.-C., and Delecluse, P. (2007). Effects of mesoscale eddies on global ocean distributions of CFC-11, CO2 and \Delta 14C. *Ocean Science*, 3(4):461–482.

Landschützer, P., Gruber, N., Bakker, D. C. E., Schuster, U., Nakaoka, S., Payne, M. R., Sasse, T. P., and Zeng, J. (2013). A neural network-based estimate of the seasonal to inter-annual variability of the Atlantic Ocean carbon sink. *Biogeosciences*, 10(11):7793–7815.

Landschützer, P., Laruelle, G. G., Roobaert, A., and Regnier, P. (2020). A uniform pCO_2 climatology combining open and coastal oceans. *Earth System Science Data*, 12(4):2537–2553.

Lauvset, S. K., Key, R. M., Olsen, A., van Heuven, S., Velo, A., Lin, X., Schirnick, C., Kozyr, A., Tanhua, T., Hoppema, M., Jutterström, S., Steinfeldt, R., Jeansson, E., Ishii, M., Perez, F. F., Suzuki, T., and Watelet, S. (2016). A new global interior ocean mapped climatology: the 1°x1° GLODAP version 2. *Earth System Science Data*, 8(2):325–340.

Levy, M., Bopp, L., Karleskind, P., Resplandy, L., Ethe, C., and Pinsard, F. (2013). Physical pathways for carbon transfers between the surface mixed layer and the ocean interior. *Global Biogeochemical Cycles*, 27(4):1001–1012.

Li, Z., England, M. H., Groeskamp, S., Cerovečki, I., and Luo, Y. (2021). The Origin and Fate of Subantarctic Mode Water in the Southern Ocean. *Journal of Physical Oceanography*.

Locarnini, R. A., Mishonov, A. V., Antonov, J. I., Boyer, T. P., Garcia, H. E., Baranova, O. K., Zweng, M. M., Paver, C. R., Reagan, J. R., Johnson, D. R., Hamilton, M., and Seidov, D. (2013). World ocean atlas 2013. Volume 1, Temperature. Publisher: U.S. Department of Commerce, National Oceanic and Atmospheric Administration, National Environmental Satellite, Data and Information Service.

Lumpkin, R. and Speer, K. (2007). Global Ocean Meridional Overturning. *Journal of Physical Oceanography*, 37(10):2550–2562.

Madec, G. (2008). NEMO ocean engine. *Institut Pierre-Simon Laplace (IPSL)*. Publisher: Zenodo.

Madec, G., Delécluse, P., Imbard, M., and Lévy, C. (1998). OPA 8.1 Ocean General Circulation Model reference manual. *Notes du pôle de mode´lisation, laboratoire d'océanographie dynamique et de climatologie, Institut Pierre Simon Laplace des sciences de l'environnement global*, 11.

Madec, G. and Imbard, M. (1996). A global ocean mesh to overcome the North Pole singularity. *Climate Dynamics*, 12(6):381–388.

Marshall, J. and Speer, K. (2012). Closure of the meridional overturning circulation through Southern Ocean upwelling. *Nature Geoscience*, 5(3):171–180.

Mathiot, P., Jenkins, A., Harris, C., and Madec, G. (2017). Explicit representation and parametrised impacts of under ice shelf seas in the z* coordinate ocean model NEMO 3.6. *Geoscientific Model Development*, 10(7):2849–2874.

Mikaloff Fletcher, S. E., Gruber, N., Jacobson, A. R., Doney, S. C., Dutkiewicz, S., Gerber, M., Follows, M., Joos, F., Lindsay, K., Menemenlis, D., Mouchet, A., Müller, S. A., and Sarmiento, J. L. (2006). Inverse estimates of anthropogenic CO $_2$ uptake, transport, and storage by the ocean: AIR-SEA EXCHANGE OF ANTHROPOGENIC CARBON. *Global Biogeochemical Cycles*, 20(2):n/a–n/a.

Mikaloff Fletcher, S. E., Gruber, N., Jacobson, A. R., Gloor, M., Doney, S. C., Dutkiewicz, S., Gerber, M., Follows, M., Joos, F., Lindsay, K., Menemenlis, D., Mouchet, A., Müller, S. A., and Sarmiento, J. L. (2007). Inverse estimates of the oceanic sources and sinks of natural CO $_2$ and the implied oceanic carbon transport: NATURAL AIR-SEA FLUXES OF CO $_2$. *Global Biogeochemical Cycles*, 21(1).

Mongwe, N. P., Vichi, M., and Monteiro, P. M. S. (2018). The seasonal cycle of pCO_2 and CO_2 fluxes in the Southern Ocean: diagnosing anomalies in CMIP5 Earth system models. *Biogeosciences*, 15(9):2851–2872.

Morrison, A. K. and McC. Hogg, A. (2013). On the Relationship between Southern Ocean Overturning and ACC Transport. *Journal of Physical Oceanography*, 43(1):140–148.

Nowicki, M., DeVries, T., and Siegel, D. A. (2022). Quantifying the Carbon Export and Sequestration Pathways of the Ocean's Biological Carbon Pump. *Global Biogeochemical Cycles*, 36(3).

Olsen, A., Key, R. M., van Heuven, S., Lauvset, S. K., Velo, A., Lin, X., Schirnick, C., Kozyr, A., Tanhua, T., Hoppema, M., Jutterström, S., Steinfeldt, R., Jeansson, E., Ishii, M., Pérez, F. F., and Suzuki, T. (2016). The Global Ocean Data Analysis Project version 2 (GLODAPv2) – an internallyconsistent data product for the world ocean. *Earth System Science Data*, 8(2):297–323.

Orr, J. C., Maier-Reimer, E., Mikolajewicz, U., Monfray, P., Sarmiento, J. L., Toggweiler, J. R., Taylor, N. K., Palmer, J., Gruber, N., Sabine, C. L., Le Quéré, C., Key, R. M., and Boutin, J. (2001). Estimates of anthropogenic carbon uptake from four three-dimensional global ocean models. *Global Biogeochemical Cycles*, 15(1):43–60.

Orr, J. C., Najjar, R. G., Aumont, O., Bopp, L., Bullister, J. L., Danabasoglu, G., Doney, S. C., Dunne, J. P., Dutay, J.-C., Graven, H., Griffies, S. M., John, J. G., Joos, F., Levin, I., Lindsay, K., Matear, R. J., McKinley, G. A., Mouchet, A., Oschlies, A., Romanou, A., Schlitzer, R., Tagliabue, A., Tanhua, T., and Yool, A. (2017). Biogeochemical protocols and diagnostics for the CMIP6 Ocean Model Intercomparison Project (OMIP). *Geoscientific Model Development*, 10(6):2169–2199.

Orsi, A. H., Whitworth, T., and Nowlin, W. D. (1995). On the meridional extent and fronts of the Antarctic Circumpolar Current. *Deep Sea Research Part I: Oceanographic Research Papers*, 42(5):641–673.

Park, Y.-H., Charriaud, E., and Fieux, M. (1998). Thermohaline structure of the Antarctic Surface Water/Winter Water in the Indian sector of the Southern Ocean. *Journal of Marine Systems*, 17(1-4):5–23.

Redi, M. H. (1982). Oceanic Isopycnal Mixing by Coordinate Rotation. *Journal of Physical Oceanography*, 12(10):1154–1158.

Resplandy, L., Lévy, M., and McGillicuddy, D. J. (2019). Effects of Eddy-Driven Subduction on Ocean Biological Carbon Pump. *Global Biogeochemical Cycles*, 33(8):1071–1084.

Rintoul, S. R. (2018). The global influence of localized dynamics in the Southern Ocean. *Nature*, 558(7709):209–218.

Rodgers, K. B., Aumont, O., Mikaloff Fletcher, S. E., Plancherel, Y., Bopp, L., De Boyer Montégut, C., Iudicone, D., Keeling, R. F., Madec, G., and Wanninkhof, R. (2014). Strong sensitivity of Southern Ocean carbon uptake and nutrient cycling to wind stirring. *Biogeosciences*, 11(15):4077–4098.

Sabine, C. L. (2004). The Oceanic Sink for Anthropogenic CO2. *Science*, 305(5682):367–371.

Sallée, J.-B., Matear, R. J., Rintoul, S. R., and Lenton, A. (2012). Localized subduction of anthropogenic carbon dioxide in the Southern Hemisphere oceans. *Nature Geoscience*, 5(8):579–584.

Sarmiento, J. L., Orr, J. C., and Siegenthaler, U. (1992). A perturbation simulation of CO $_2$ uptake in an ocean general circulation model. *Journal of Geophysical Research*, 97(C3):3621.

Sauvé, J., Gray, A., Prend, C. J., Bushinsky, S. M., and Riser, S. (2023). Carbon outgassing in the Antarctic Circumpolar Current is supported by Ekman transport from the sea ice zone in an observation-based seasonal mixed-layer budget. preprint, Preprints.

Stukel, M. R. and Ducklow, H. W. (2017). Stirring Up the Biological Pump: Vertical Mixing and Carbon Export in the Southern Ocean: Vertical Mixing and Carbon Export in SO. *Global Biogeochemical Cycles*, 31(9):1420–1434.

Stukel, M. R., Irving, J. P., Kelly, T. B., Ohman, M. D., Fender, C. K., and Yingling, N. (2023). Carbon sequestration by multiple biological pump pathways in a coastal upwelling biome. *Nature Communications*, 14(1):2024.

Szekely, T., Gourrion, J., Pouliquen, S., and Reverdin, G. (2019). The CORA 5.2 dataset for global in situ temperature and salinity measurements: data description and validation. *Ocean Science*, 15(6):1601–1614.

Talley, L. D. (2013). Closure of the Global Overturning Circulation Through the Indian, Pacific, and Southern Oceans: Schematics and Transports. *Oceanography*, 26(1):80–97.

Tamsitt, V., Drake, H. F., Morrison, A. K., Talley, L. D., Dufour, C. O., Gray, A. R., Griffies, S. M., Mazloff, M. R., Sarmiento, J. L., Wang, J., and Weijer, W. (2017). Spiraling pathways of global deep waters to the surface of the Southern Ocean. *Nature Communications*, 8(1):172.

Terhaar, J., Frölicher, T. L., and Joos, F. (2021). Southern Ocean anthropogenic carbon sink constrained by sea surface salinity. *Science Advances*, 7(18):eabd5964.

Terhaar, J., Orr, J. C., Gehlen, M., Ethé, C., and Bopp, L. (2019). Model constraints on the anthropogenic carbon budget of the Arctic Ocean. *Biogeosciences*, 16(11):2343–2367.

Thompson, A. F. and Sallée, J.-B. (2012). Jets and Topography: Jet Transitions and the Impact on Transport in the Antarctic Circumpolar Current. *Journal of Physical Oceanography*, 42(6):956–972.

Toyama, K., Rodgers, K. B., Blanke, B., Iudicone, D., Ishii, M., Aumont, O., and Sarmiento, J. L. (2017). Large Reemergence of Anthropogenic Carbon into the Ocean's Surface Mixed Layer Sustained by the Ocean's Overturning Circulation. *Journal of Climate*, 30(21):8615–8631.

Vancoppenolle, M., Fichefet, T., and Goosse, H. (2009). Simulating the mass balance and salinity of Arctic and Antarctic sea ice. 2. Importance of sea ice salinity variations. *Ocean Modelling*, 27(1-2):54–69.

Wanninkhof, R. (1992). Relationship between wind speed and gas exchange over the ocean. *Journal of Geophysical Research*, 97(C5):7373.

Williams, N. L., Juranek, L. W., Feely, R. A., Johnson, K. S., Sarmiento, J. L., Talley, L. D., Dickson, A. G., Gray, A. R., Wanninkhof, R., Russell, J. L., Riser, S. C., and Takeshita, Y. (2017). Calculating surface ocean pCO $_2$ from biogeochemical Argo floats equipped with pH: An uncertainty analysis: Calculating Ocean pCO $_2$ From Float pH. *Global Biogeochemical Cycles*, 31(3):591–604.

Zweng, M. M., Reagan, J. R., Antonov, J. I., Locarnini, R. A., Mishonov, A. V., Boyer, T. P., Garcia, H. E., Baranova, O. K., Johnson, D. R., Seidov, D., and Biddle, M. M. (2013). World ocean atlas 2013. Volume 2, Salinity. Publisher: U.S. Department of Commerce, National Oceanic and Atmospheric Administration, National Environmental Satellite, Data and Information Service.

Chapter 7

Appendices

7.1 Supplementary figures

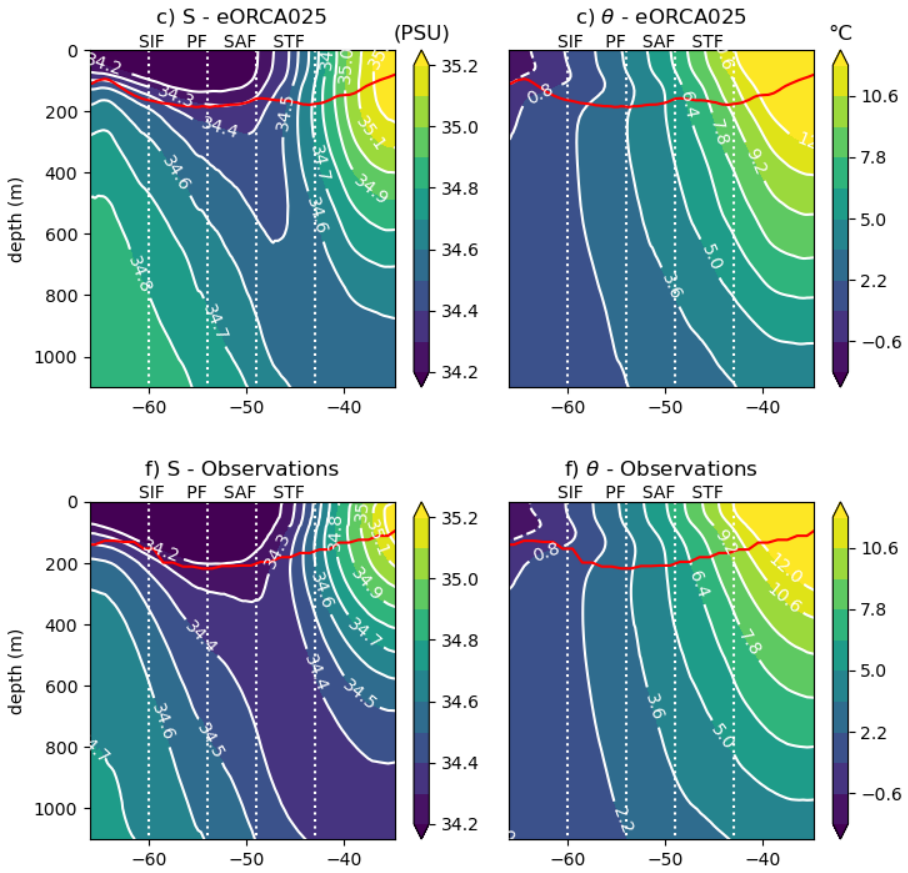

Figure S1: Zonally averaged cross-sections for (a,c) salinity and (b,d) potential temperature in (a,b) our model and (c,d) in observations (Szekely et al., 2019). The mixed layer is represented by a red line for our model (a,b) and observations (c,d) (Hosoda et al., 2010).

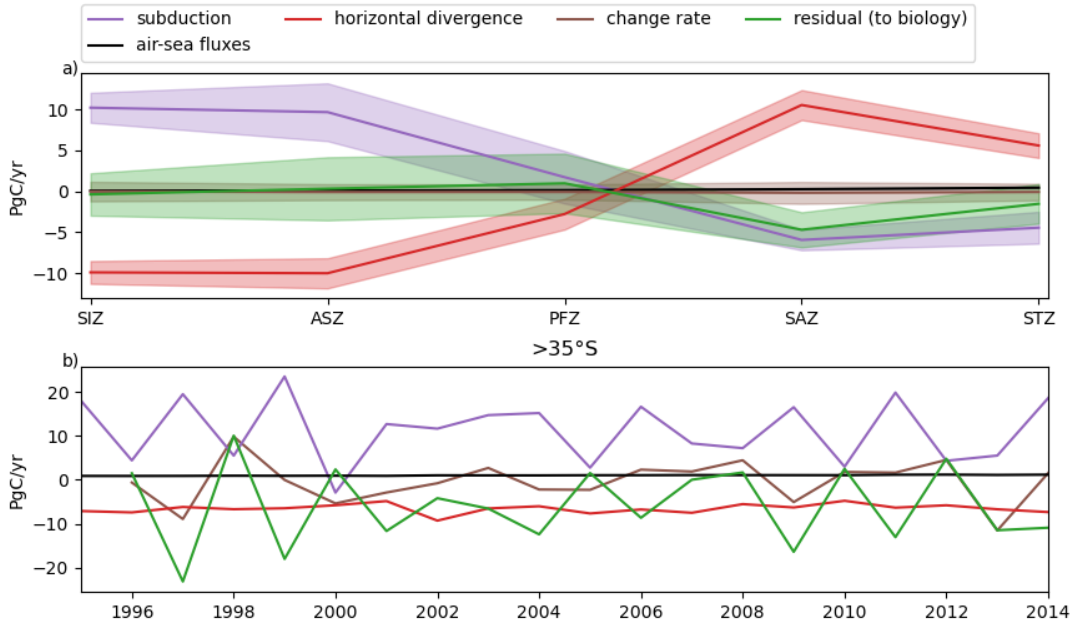

Figure S2: Interannual variability for historical DIC physical transfer. a) Interannual variability per region. The thick line corresponds to the average over 1995-2014, while the shaded area corresponds to the 20 years variability. b) Times series of the different physical transfer processes for the SO. Positive values represent obduction.

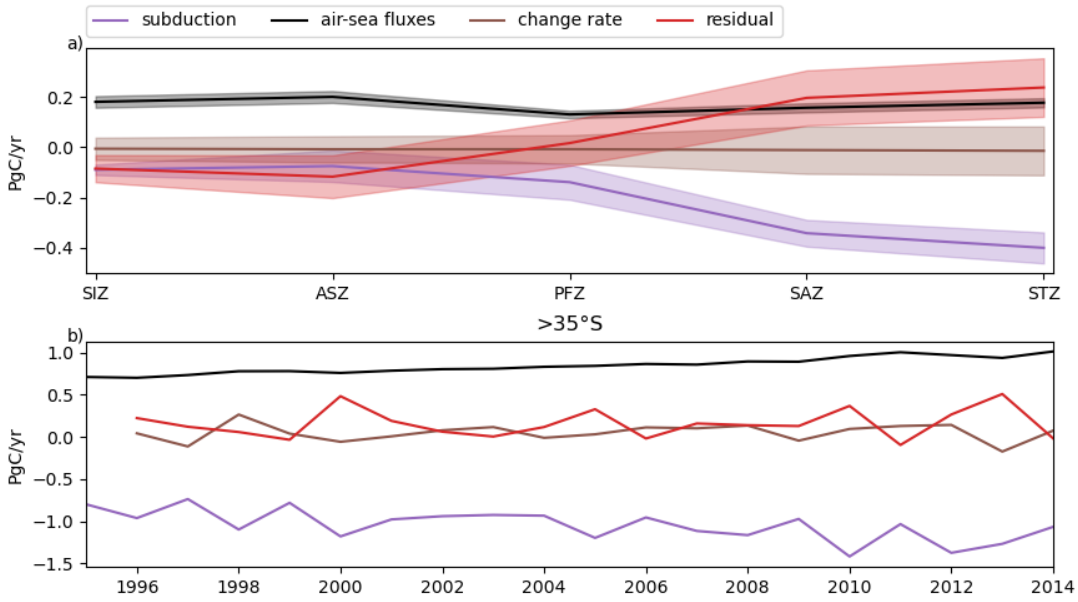

Figure S3: Same as Fig.S2 but for anthropogenic DIC.

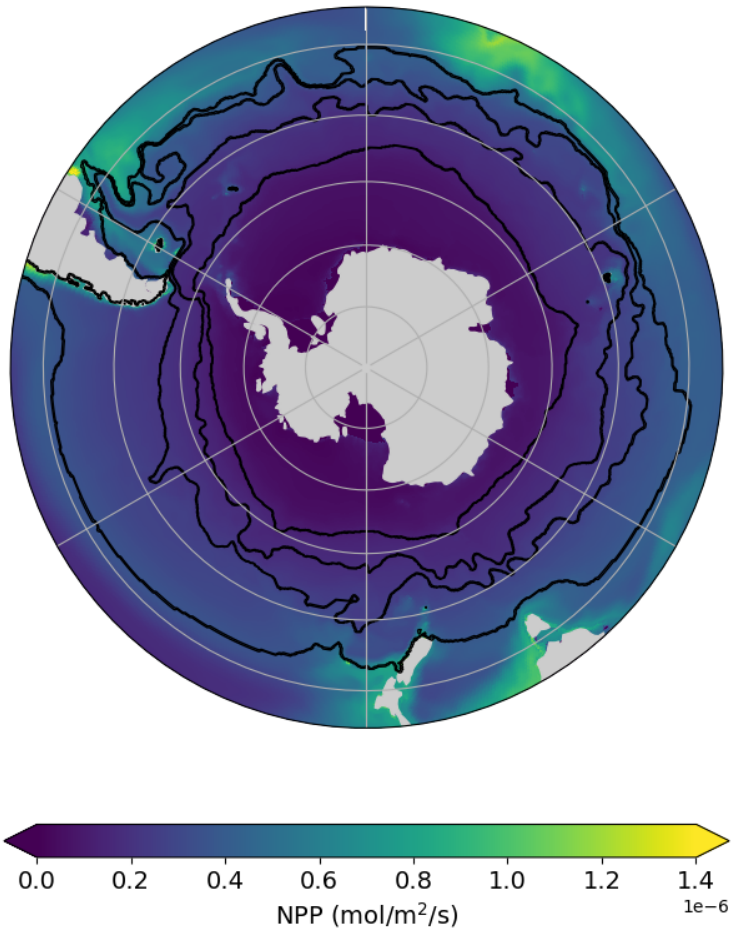

Figure S4: Net primary production averaged over 1995-2014.

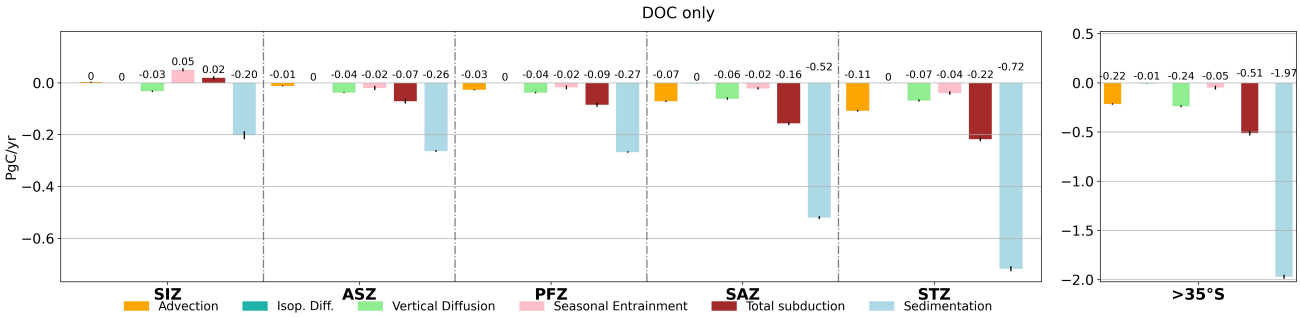

Figure S5: Same as Fig.3.7 but with only DOC physical transfer.

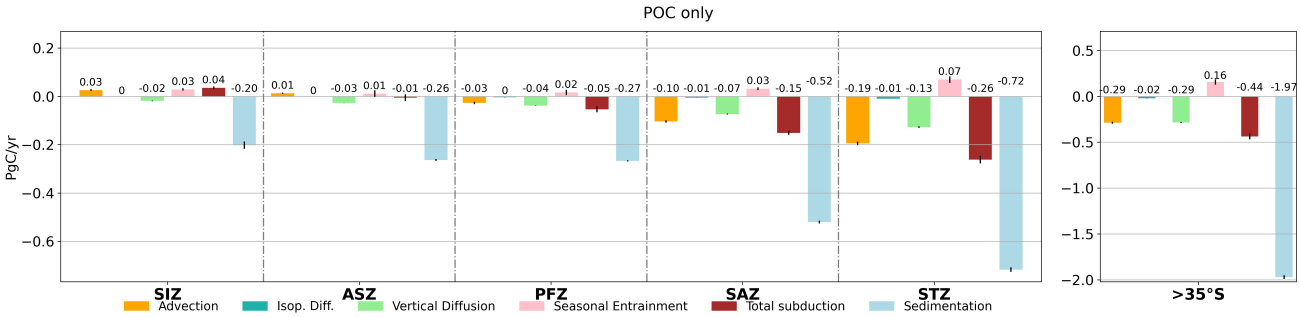

Figure S6: Same as Fig.3.7 but with only POC physical transfer.

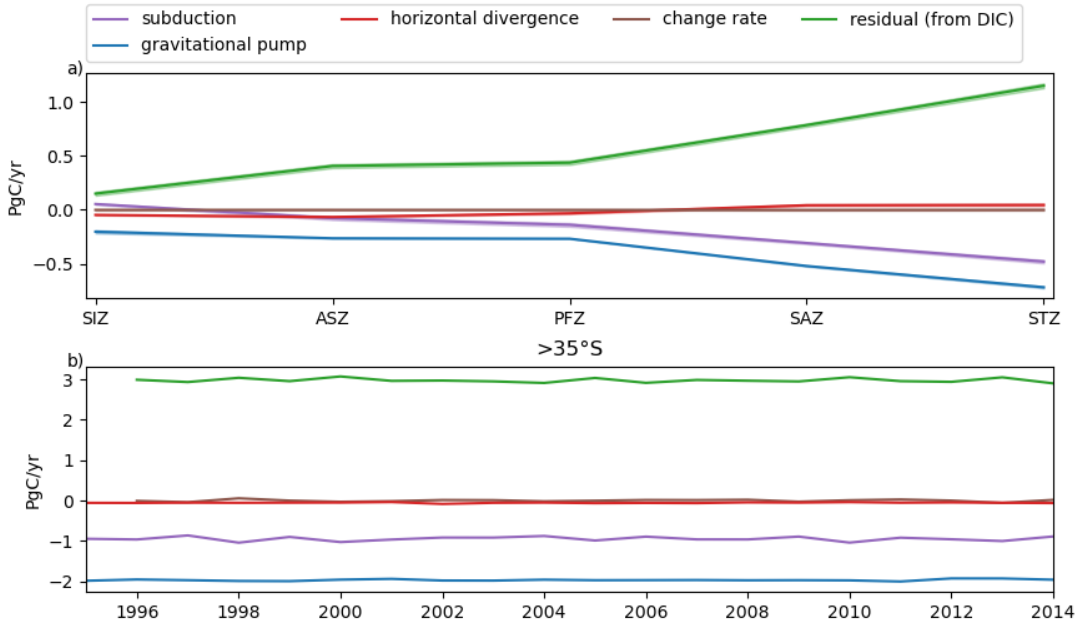

Figure S7: Same as Fig.S2 but for TOC.

7.2 Comparisons with the results from the SOLACE campaign

The SOLACE campaigns occurred in December 2020 and January 2021 in the south of Tasmania, next to the Subtropical Front (region of high EKE). They aimed to give a better understanding of the organic carbon pumps at a small scale. We collaborated in this project by giving regional estimates of the larger-scale pump based on the output of the eORCA025-PISCES model. We describe in Fig.S8 the subduction of POC and the gravitational pump in the region of the campaign, with two subregions "SOUTH" and "SOTS". We conclude that in our simulations, the subduction represents a very small part of the gravitational pump (Fig.3.7), as subduction in December and obduction in January from the seasonal entrainment and the vertical diffusion compensate (not shown). Maximum seasonal entrainment corresponding to a large shoaling of the mixed layer is however higher than the gravitational pump in November. Over the year, subduction represents however half of the gravitational pump in this region (not shown), which is in line with the results described in Section 3.3.

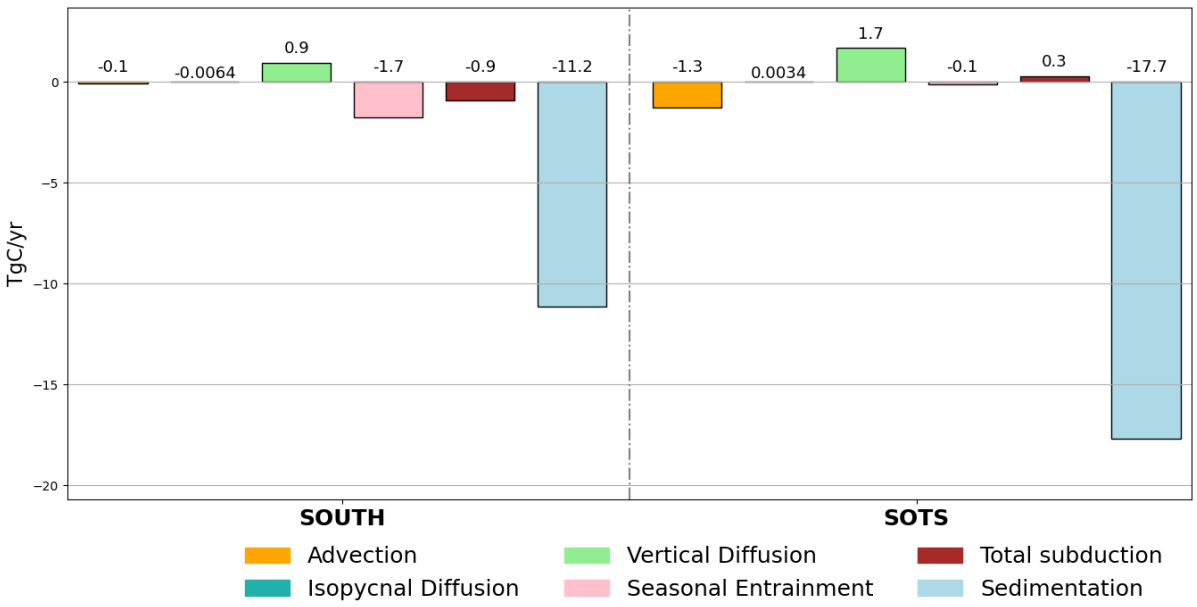

Figure S8: Decomposition of subduction POC fluxes across the base of the mixed layer averaged over for January and December 1995-2014 for the zones SOUTH and SOTS. Same convention as in Fig.3.7.b).

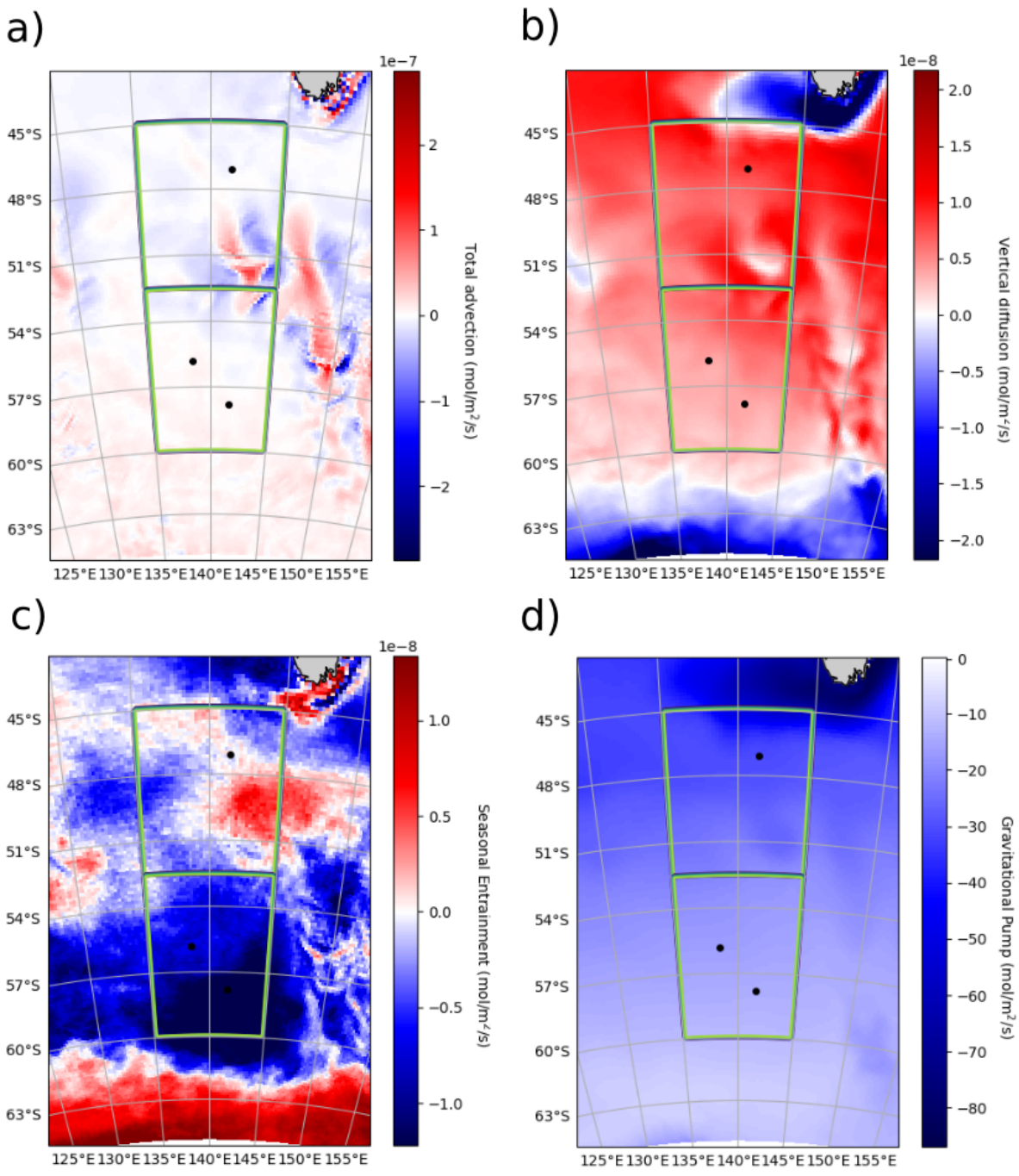

Figure S9: Maps of POC fluxes averaged on January-December 1995-2014: a) total advection, b) vertical diffusion c) seasonal entrainment d) gravitational pump. Positive fluxes correspond to obduction. Green squares correspond to SOTS (north) and SOUTH (south). The three black dots correspond to the three stations, from north to south SOTS, SOUTH1 and SOUTH2.

7.3 Hotspots of inorganic and organic carbon fluxes - preliminary results

At the local scale, regions of maximal eddy kinetic energy (EKE) are linked with enhanced DIC vertical advection and mixing, creating strong local subduction, or "subduction hotspots" (Balwada et al., 2018; Dove et al., 2021). High eddy activity at topographic hotspots also leads to localized enhanced upwelling of natural DIC and possibly enhanced obduction at the mixed layer base (Brady et al., 2021). Resolving the mesoscale and thereby allowing those hotspots' existence could significantly change the tracer budget at the mixed layer base (Rintoul, 2018; Thompson and Sallée, 2012).

Here, we attempt to identify and quantify the hotspots of carbon subduction in the model. To do so, hotspots are defined with two methodologies used mostly for geoanalysis, found in https://geographicdata.science/book/notebooks/07_local_autocorrelation.html:

1. the Getis-Ord Gi* spatial statistics, which detect spatial clusters with statistically significant high absolute values. This part is not presented here.

2. the cluster and outlier analysis, or Moran's I, which measures the local spatial autocorrelation with neighbours of high (absolute) values.

With Moran's I method, we compute the significant outliers (hotspots) of our total advection averaged from 1995 to 2014 for DIC_{hist}. We first remove the values fifteen times more important than the standard deviation over all the regions, which are too important (stronger fluxes in coastal regions) to be taken into account in our analysis. We also remove the sea ice zone, where the hotspots could be attributed to other phenomena (coastal, ice melting) and therefore should not be associated with the other regions. We then obtain points reported into 5 categories: the first one are not significant outliers with a 5% significant level, the second one, HH, are obductive (positive) outliers which also have obductive neighbours, the third one, LH, are subductive outliers with obductive neighbours, the fourth one, LL, are subductive outliers with subductive neighbours, and the fifth one, HL, are obductive outliers with subductive neighbours.

The results of the hotspots detection are represented in Fig.S10. We observe that hotspots follow the patterns of high EKE regions such as the ACC and the strong boundary currents. Most outliers have neighbours with similar behaviors. Table 7.3 indicates that for obduction (subduction), hotspots account for 65% (58%) of the total obduction, while only representing 17% of the area.

Table S1: Obductive and subductive hotspots. Obduction/subduction for each kind of outliers are divided by the total obduction/subduction

Category	HH	LH	LL	HL	Total
Area (%)	9.0	0.6	7.4	0.6	17
Obduction (%)	61	0	0	4	65
Subduction (%)	0	3	55	0	58

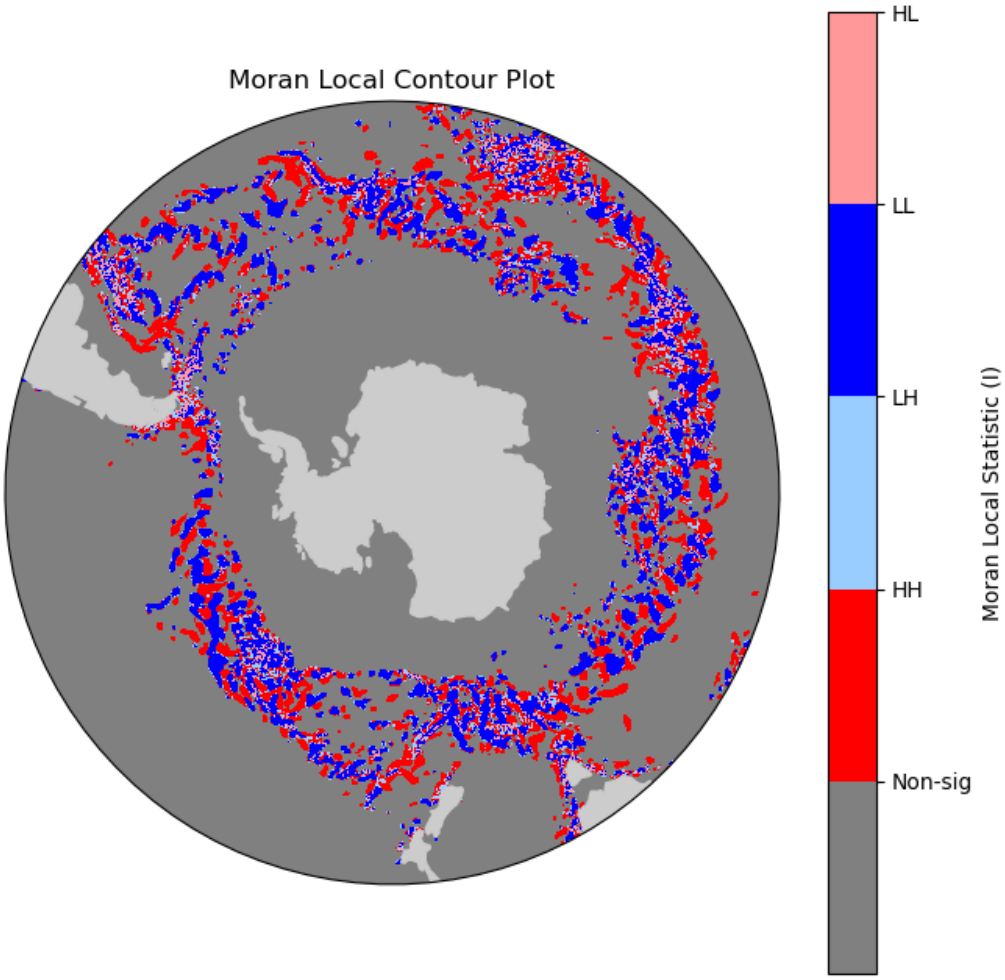

Figure S10: Map of hotspots for DIC_{hist} total advection, averaged over 1995-2014.